

NASA/TM-2012-217790



# Progressive Damage Analysis of Bonded Composite Joints

*Frank A. Leone, Jr.*  
*Langley Research Center, Hampton, Virginia*

*Donato Girolamo*  
*Delft University of Technology, Delft, Netherlands*

*Carlos G. Dávila*  
*Langley Research Center, Hampton, Virginia*

## NASA STI Program . . . in Profile

Since its founding, NASA has been dedicated to the advancement of aeronautics and space science. The NASA scientific and technical information (STI) program plays a key part in helping NASA maintain this important role.

The NASA STI program operates under the auspices of the Agency Chief Information Officer. It collects, organizes, provides for archiving, and disseminates NASA's STI. The NASA STI program provides access to the NASA Aeronautics and Space Database and its public interface, the NASA Technical Report Server, thus providing one of the largest collections of aeronautical and space science STI in the world. Results are published in both non-NASA channels and by NASA in the NASA STI Report Series, which includes the following report types:

- **TECHNICAL PUBLICATION.** Reports of completed research or a major significant phase of research that present the results of NASA Programs and include extensive data or theoretical analysis. Includes compilations of significant scientific and technical data and information deemed to be of continuing reference value. NASA counterpart of peer-reviewed formal professional papers, but having less stringent limitations on manuscript length and extent of graphic presentations.
- **TECHNICAL MEMORANDUM.** Scientific and technical findings that are preliminary or of specialized interest, e.g., quick release reports, working papers, and bibliographies that contain minimal annotation. Does not contain extensive analysis.
- **CONTRACTOR REPORT.** Scientific and technical findings by NASA-sponsored contractors and grantees.

- **CONFERENCE PUBLICATION.** Collected papers from scientific and technical conferences, symposia, seminars, or other meetings sponsored or co-sponsored by NASA.
- **SPECIAL PUBLICATION.** Scientific, technical, or historical information from NASA programs, projects, and missions, often concerned with subjects having substantial public interest.
- **TECHNICAL TRANSLATION.** English-language translations of foreign scientific and technical material pertinent to NASA's mission.

Specialized services also include organizing and publishing research results, distributing specialized research announcements and feeds, providing information desk and personal search support, and enabling data exchange services.

For more information about the NASA STI program, see the following:

- Access the NASA STI program home page at <http://www.sti.nasa.gov>
- E-mail your question to [help@sti.nasa.gov](mailto:help@sti.nasa.gov)
- Fax your question to the NASA STI Information Desk at 443-757-5803
- Phone the NASA STI Information Desk at 443-757-5802
- Write to:  
STI Information Desk  
NASA Center for AeroSpace Information  
7115 Standard Drive  
Hanover, MD 21076-1320

NASA/TM-2012-217790



# Progressive Damage Analysis of Bonded Composite Joints

*Frank A. Leone, Jr.*  
*Langley Research Center, Hampton, Virginia*

*Donato Girolamo*  
*Delft University of Technology, Delft, Netherlands*

*Carlos G. Dávila*  
*Langley Research Center, Hampton, Virginia*

National Aeronautics and  
Space Administration

Langley Research Center  
Hampton, Virginia 23681-2199

December 2012

The use of trademarks or names of manufacturers in this report is for accurate reporting and does not constitute an official endorsement, either expressed or implied, of such products or manufacturers by the National Aeronautics and Space Administration.

Available from:

NASA Center for AeroSpace Information  
7115 Standard Drive  
Hanover, MD 21076-1320  
443-757-5802

# Progressive Damage Analysis of Bonded Composite Joints

Frank A. Leone, Jr.<sup>1</sup>; Donato Girolamo<sup>2</sup>; Carlos G. Dávila<sup>1</sup>

<sup>1</sup> NASA Langley Research Center, Hampton, VA

<sup>2</sup> Delft University of Technology, Delft, NL

## Abstract

---

The development of durable bonded joint technology for assembling composite structures for launch vehicles is being pursued as a component of the U.S. Space Launch System. The present work is related to the development and application of progressive damage modeling techniques to bonded joint technology, applicable to a wide range of sandwich structures for a Heavy Lift Launch Vehicle. The joint designs studied in this work include a conventional composite splice joint and a NASA-patented durable redundant joint. Both designs involve honeycomb sandwich structures with carbon/epoxy facesheets joined using adhesively bonded doublers.

Progressive damage modeling allows for the prediction of the initiation and evolution of damage within a structure. For structures that include multiple material systems, such as the joint designs under consideration, the number of potential failure mechanisms that must be accounted for drastically increases the complexity of the analyses. Potential failure mechanisms include fiber fracture, intraply matrix cracking, delamination, core crushing, adhesive failure, and their interactions. The bonded joints were modeled using highly parametric, explicitly solved finite element models, with damage modeling implemented via custom user-written subroutines. Each ply was discretely meshed using three-dimensional solid elements. Layers of cohesive elements were included between each ply to account for the possibility of delaminations and were used to model the adhesive layers forming the joint. Good correlation with experimental results was achieved both in terms of load-displacement history and the predicted failure mechanism(s).

## **Acknowledgments**

---

The present report represents the author's contribution to an activity that was only possible with the combined efforts of many individuals. The authors would like to thank our team manager, Dr. Shih-Yung Lin, who led the design, testing, and analysis efforts with energy and good humor. The panel tests were conducted with particular care and precision by Scott Splinter. Summer intern Andy Renwick helped process the VIC-3D digital image correlation data. Special credit is deserved by Dr. James Ratcliffe, who provided the fixtures and assistance for the experimental adhesive characterization. We also thank Patrick O'Neill for his expert advice on VIC-3D. Finally, no research can take place without advocacy and funding. Dr. Stanley Smeltzer has always pushed for the development of joints and related analysis technology and it is his successful efforts in this regard that allowed this effort to proceed.

## Table of Contents

1	Introduction.....	1
2	Configuration of the Panels and Joints .....	1
3	Progressive Damage Analysis Methods.....	3
3.1	Continuum Damage Mechanics .....	3
3.2	Cohesive Zone Modeling .....	3
3.3	Core Crush Model.....	4
4	Material Properties.....	4
4.1	TE-1, Grade 190, Type 35, Prepreg Tape .....	5
4.2	Honeycomb Core .....	5
4.3	Characterization of FM-300M Adhesive .....	6
4.3.1	Experimental Tests.....	6
4.3.2	Cohesive Laws for Adhesive .....	11
4.3.3	Adhesive Material Properties for the Composite Joint Models .....	16
4.3.4	Finite Element Models of Characterization Specimens .....	17
4.3.5	Double Delamination .....	18
5	Finite Element Models of Bonded Composite Joints.....	20
5.1	Pristine Sandwich Panel.....	21
5.2	Conventional Splice Joint (CSJ) .....	21
5.3	Durable Redundant Joint (DRJ).....	23
6	Results of Bonded Composite Joint Models .....	25
6.1	Strength Predictions and Failure Mechanisms .....	25
6.1.1	Analyses of Pristine Sandwich Panels .....	25
6.1.2	Analyses of Conventional Splice Joints.....	28
6.1.3	Analyses of Durable Redundant Joints .....	32
6.2	Effect of the Teflon Insert Length on the Conventional Splice Joint Strength .....	35
7	Closing Remarks .....	37

# 1 Introduction

Finite element analyses were conducted to investigate the mechanical response and strength of two design concepts for joining composite sandwich panels. The first joint consists of a conventional splice joint (CSJ), and the second concept is referred to as the Durable Redundant Joint (DRJ). In this study, the strength and failure modes of both joint designs are compared to those of the pristine sandwich for tension and compression loading.

In total, progressive damage analyses (PDA) were conducted for six joint configurations:

- Pristine panel, tensile loading
- Pristine panel, compressive loading
- Conventional splice joint, tensile loading
- Conventional splice joint, compressive loading
- Durable redundant joint, tensile loading
- Durable redundant joint, compressive loading

All simulations account for several potential failure modes, including intralaminar damage of the graphite/epoxy facesheets and splices, compression damage in the honeycomb core, failure of the adhesive layers, and interply delaminations. The results gathered from these analyses are presented herein.

## 2 Configuration of the Panels and Joints

The pristine sandwich panels used in this study are composed of six-ply carbon/epoxy facesheets and a one-inch-thick aluminum honeycomb core, as shown in Figure 1a. The facesheet plies have a nominal thickness of 0.0075 inch. The stacking sequence of the facesheets is [+60/0/-60]<sub>s</sub>. The tensile pristine panels (Pristine\_Tnsn\_#) are 22 inches long and 3 inches wide, with the 0° direction aligned with the specimen length. The compressive pristine panel specimens each measure 12 inches long and 7 inches wide. The compressive pristine panel specimens were tested in two configurations: with the 0° direction parallel to the specimen length (i.e., Pristine\_Cmpr\_L\_#), and with the 0° direction parallel to the specimen width (i.e., Pristine\_Cmpr\_T\_#).

The conventional splice joint (CSJ) specimens consist of two pristine sandwich panel sections joined with two 2.75-inch-long, six-ply splices bonded to the exterior faces of the sandwich with FM-300M adhesive, Figure 1b. At their thickest, the splices have the same stacking sequence as the facesheets. The splices have internal ply terminations and ply drops, and the cascading ply terminations are separated by 0.25 inches from each other. Like the pristine panel specimens, the tensile CSJ specimens (CSJ\_Tnsn\_#) measure 22 inches long and 3 inches wide, while the compressive specimens (CSJ\_Cmpr\_L\_#) are 12 inches long and 7 inches wide.

Design specifications for the joint specimens allow for a 0.10-inch gap between the sandwich panels, although it was assumed that the two sandwich panels are initially in contact. To decrease the severity of the stress concentration in the splice near the gap of a CSJ, the 0.50-inch Teflon film was inserted in-line with the adhesive layer at the joint gap. The effect of changing the length of the Teflon insert on the strength of the joint was explored using the progressive damage modeling tools.

The durable redundant joint (DRJ) concept expands upon the design of the conventional splice joints by adding three hollow laminated inserts in place of honeycomb core at the joint center, Figure 1c. These inserts increase the damage tolerance of the joints by providing an additional load path within the joint. In addition, the inserts cause a nearly symmetrical load path across the joint, which reduces the bending of the facesheets and the associated peel stresses. The DRJ inserts were bonded to the interior surface of the sandwich facesheets using the same FM-300M adhesive as for the splices.

A summary of the specimen geometries and orientations can be found in Table 1.

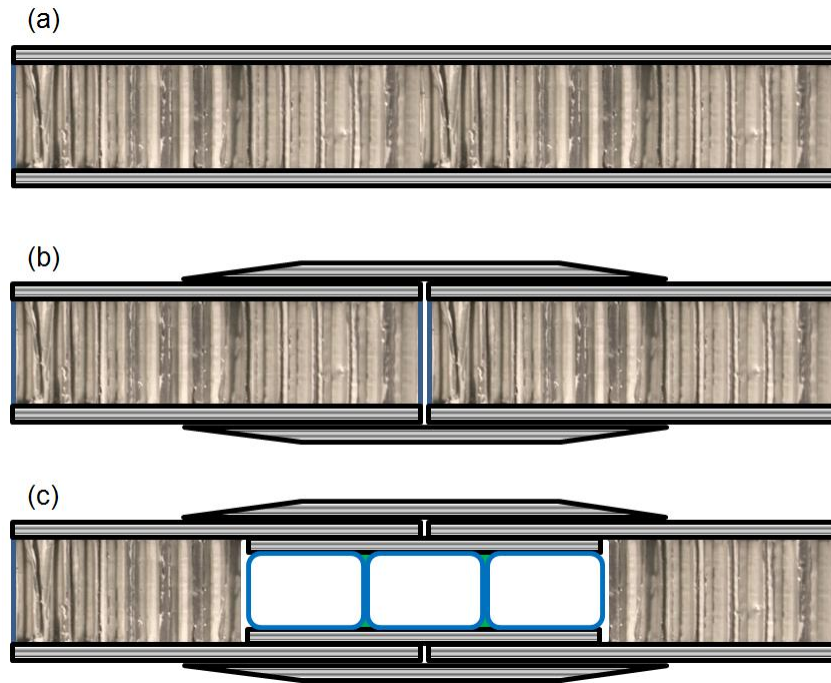


Figure 1. Schematics of the (a) pristine sandwich, (b) conventional splice joint, and (c) durable redundant joint.

Table 1. Experimental Specimen Geometries and Orientations.

<b>Specimen Name</b>	<b>Length [in.]</b>	<b>Width [in.]</b>	<b>Orientation of 0° plies</b>
Pristine_Tnsn_#	22	3	Length
Pristine_Cmpr_L_#	12	7	Length
Pristine_Cmpr_T_#	12	7	Width
CSJ_Tnsn_#	22	3	Length
CSJ_Cmpr_L_#	12	7	Length
DRJ_Tnsn_#	22	3	Length
DRJ_Cmpr_L_#	12	7	Length

### **3 Progressive Damage Analysis Methods**

As with any composite structure, the sandwich panel joints considered herein have the potential to exhibit several simultaneous failure mechanisms. For example, fiber fracture and intraply matrix cracking can occur within the carbon/epoxy plies, mixed-mode delaminations are possible between the plies, the adhesive can debond, and the honeycomb sandwich core can crush. Each of these possible failure mechanisms has the potential to interact with any other mechanism. In order to account for each of these potential failure mechanisms and their many possible interactions, multiple progressive damage modeling methodologies were required. Intraply damage was taken into account via a continuum damage mechanics (CDM) approach. Interply and adhesive damage was implemented via the inclusion of layers of cohesive elements. Honeycomb core crushing was modeled using a specialized one-dimensional damage model. The next sub-sections briefly describe the progressive damage modeling techniques that were used in the present analyses.

#### **3.1 Continuum Damage Mechanics**

Continuum damage mechanics is a progressive damage modeling approach that allows for the predictions of both damage initiation and evolution without having to make modifications to the original finite element mesh of the structure being analyzed. Rather than modeling cracks by the discrete insertion of discontinuities into the original finite element mesh, CDM approaches represent the effects of cracks by softening certain components of the constitutive stiffness tensor. Different damage modes are accounted for with a set of scalar damage state variables. After the initiation of damage, the affected stiffness terms are softened according to relevant fracture toughness properties and the local characteristic element size. As a result, in order to accurately predict the initial linear elastic response, the initiation of damage, and the evolution of damage, it is necessary to have a set of material property data including the elastic moduli, strengths and fracture toughness values for each potential failure mechanism.

For the prediction of intraply damage initiation, a combination of the LaRC03 [1] and LaRC04 [2] failure criteria were used in this work. The LaRC set of criteria consists of stress-based analytical equations that predict the onset of failure mechanisms such as matrix cracking, fiber fracture, and fiber kinking. The prediction of damage evolution was implemented through an updated version of the CDM approach originally proposed by Maimí et al. [3]. The improvements to the CDM approach that are relevant to this work include: (1) an extension of the set of failure criteria to account for three-dimensional stress states, as well as extensions to the corresponding damage evolution laws and stiffness tensor degradation algorithms; (2) the development of a mixed-mode matrix damage evolution law [4]; and (3) the development of a new definition for the CDM effective stresses that allow for the simultaneous evolution of multiple damage modes. The application of this CDM method to this work allowed for the prediction of fiber and matrix damage in the joint models due to tensile, compressive, and/or shear loading.

#### **3.2 Cohesive Zone Modeling**

Layers of zero-thickness cohesive elements were used between all plies of different orientations to account for the potential of delaminations developing between plies. Cohesive elements are specialized nonlinear finite elements that are particularly useful to predict the initiation and evolution of cracks when

the potential propagation paths are known a priori, such as is the case with delamination planes, e.g., Turon et al. [5].

The constitutive response of cohesive elements is defined using a so-called cohesive law, defined in terms of local traction versus crack opening displacement. Prior to the prediction of damage initiation, a high cohesive stiffness keeps the crack surfaces closed. Upon satisfying a failure criterion, the stiffness properties of the element soften with further deformation until the element has completely failed. The crack opening displacements corresponding to damage initiation and complete failure are dependent on the pure mode I and mode II strengths and fracture toughness values, as well as the local mode mixity. Cohesive elements only have stiffness terms related to the normal and tangential directions to the potential fracture plane and, as such, no in-plane loads can be carried by the elements.

In the present work, cohesive elements were also used in a novel approach to represent the response and failure of the adhesive layer. When used in this mode, the cohesive elements have the true thickness and the compliance of the adhesive layer. The cohesive laws that describe the initial stiffness, the failure, and the softening of the adhesive were determined experimentally using a procedure described in Section 4.3.

### **3.3 Core Crush Model**

To represent the loss of stiffness of a honeycomb core as a result of crushing under compressive normal loads, a custom one-dimensional material model was used [6]. This damage model separates the compressive normal response of a honeycomb material into three parts: (1) the initial linear-elastic response, characterized by the Young's modulus; (2) the crushing of the core, during which the material has a negative tangent stiffness; and (3) post-crushed response, characterized by a significantly reduced modulus. In addition, the core crush damage model is capable of representing the unloading/reloading response of either a partially or fully crushed material.

This damage model is one-dimensional—it represents only the direction perpendicular to the core. Therefore, this model is not designed to represent the transverse shear response of the honeycomb core.

## **4 Material Properties**

As for any analysis, the reliability of predictions obtained with progressive damage analyses can only be as good as the quality of the input material properties. While the errors in the predictions of failure in linear analyses are likely to be of a magnitude comparable to the uncertainty in the input strength data, the errors in progressive damage analyses can exhibit a much greater sensitivity to incorrect material properties, especially for structures that exhibit multiple damage modes and extensive damage evolution before ultimate structural failure. As a result, it is strongly recommended to use reliable material strength and fracture toughness properties for progressive damage analyses when available, and, to independently characterize the materials of interest when possible.

Unfortunately, progressive damage analysis models often require material data that is not available, and cost and scheduling constraints prevent the undertaking of a thorough material characterization. Such is the case for the present effort. Furthermore, the composite material used in the fabrication of the panels is a proprietary material of The Boeing Company that is only known to be a toughened epoxy TE-1 Grade 190 Type 35 prepreg tape similar to T800/977-2. Consequently, the material properties used herein were assembled from several sources, and, for those properties that were not available, the corresponding

properties of a similar material were used. The following sections outline all of the material properties needed to conduct the progressive damage analyses of the joint specimens as well as the source of each property.

#### 4.1 TE-1, Grade 190, Type 35, Prepreg Tape

The material properties used for the TE-1 carbon/epoxy plies in the facesheets and doublers are shown in Table 2. The elastic, thermal, and strength properties were provided by The Boeing Company [7]. The mode I and mode II matrix fracture toughness properties,  $G_{YT}$  and  $G_{SL}$ , and Benzeggagh-Kenane mixed-mode factor  $\eta$ , are those of IM7/977-2, published by Reeder [8]. These properties were used for the prediction of both intraply matrix cracking and interply delaminations. The availability of fiber fracture toughness properties,  $G_{XT}$  and  $G_{XC}$ , is extremely limited in the literature. As a result, the well-documented fiber fracture toughness properties of IM7/8552, another toughened epoxy system of similar performance, were used in this investigation.

Table 2. TE-1 Grade 190 Type 35 Carbon/Epoxy tape Material Properties.

<b>Elastic Properties</b>			<b>Strength Properties</b>			<b>Fracture Properties</b>		
$E_{11}$	20.6	Msi	$X_T$	378.	ksi	$G_{XT}^*$	838.	lbf/in
$E_{22}$	1.13	Msi	$f_{XT}^*$	0.069		$f_{GXT}^*$	0.822	
$E_{33}$	1.13	Msi	$X_C$	-244.	ksi	$G_{XC}^*$	607.	lbf/in
$G_{12}$	0.58	Msi	$f_{XC}^*$	0.069		$f_{GXC}^*$	0.822	
$G_{13}$	0.58	Msi	$Y_T$	10.5	ksi	$G_{YT}^\ddagger$	1.5	lbf/in
$G_{23}$	0.40	Msi	$Y_C$	-43.3	ksi	$G_{YC}^\ddagger$	13.3	lbf/in
$\nu_{12}$	0.34		$S_L$	16.8	ksi	$G_{SL}^\ddagger$	8.0	lbf/in
$\nu_{13}$	0.34		$S_T^\ddagger$	16.3	ksi	$\eta^*$	1.4	
$\nu_{23}$	0.40							
<b>Thermal Properties</b>								
$\alpha_{11}$	0.02e-6	/°F						
$\alpha_{22}$	18.0e-6	/°F						
$\alpha_{33}$	18.0e-6	/°F						

\* IM7/8552 properties [9, 10].

† Calculated

‡ IM7/977-2 properties [8].

#### 4.2 Honeycomb Core

The aluminum honeycomb material used in the panels and bonded joint specimens is Hexcel CR III 1/8-5052-.0007, whose manufacturer-supplied material properties can be found in Table 3. Of the available properties, only the thickness-direction modulus and strength were needed for the core crush damage model used in this study.

Several of the stresses and strains required to fully characterize the honeycomb material according to the damage model were not available. As a result, assumptions were made regarding the behavior of the honeycomb material after the initiation of the crushing failure mechanism. By analogy with other aluminum honeycomb cores, it was assumed that after exceeding its compressive strength, the core would

crush and the reaction load would drop by half, to  $-150$  psi and at  $-0.8\%$  deformation. Further compression of the core would cause the load to increase gradually with a tangent stiffness equal to one percent of the initial stiffness, i.e.,  $0.75$  ksi. It was found that the predicted results were relatively insensitive to the material properties related to the post-crush response.

Table 3. Hexcel CR III 1/8-5052-.0007 Honeycomb Material Properties.

<b>Elastic Properties</b>		<b>Strength Properties</b>	
$E_{33}$	75. ksi	$X_{33}$	$-300.$ psi
$G_{\text{ribbon}}$	45. ksi		
$G_{\text{trans.}}$	22. ksi		

### 4.3 Characterization of FM-300M Adhesive

Prior to beginning this study, there was no satisfactory source for the strength and fracture properties for the specific adhesive and adhesive thickness used in this test program. Due to the importance of these material properties for a bonded joint analysis, a thorough characterization study was conducted. In addition, because of the expected highly nonlinear behavior of the adhesive, it was necessary to develop a novel means of representing the initial failure and softening of the adhesive material in the joint finite element models.

This characterization study consisted of experimentally measuring the load response of bonded coupon structures, calculating the local material softening responses, and developing a means to represent this response in a finite element model using commercially available cohesive elements.

#### 4.3.1 Test Specimens for Adhesive Characterization

The fracture toughness, i.e., the critical energy release rate (CERR), is an essential material property for predicting debonding and crack propagation. The American Society for Testing and Materials (ASTM) advocates the use of several standard procedures to assess the toughnesses in mode I and mixed mode I/II. The Double Cantilever Beam (DCB) specimen is used to characterize the mode I fracture toughness (ASTM D 5528-01 [11], Figure 2a), and the Mixed-Mode Bending (MMB) specimen is used for mixed-mode (ASTM D 6671/D 6671M-06 [12], Figure 2c). Researchers are also working to standardize a procedure for the mode II delamination with tests such as the End-Notched Flexure (ENF) specimen (ASTM Work Item WK22949 [13], Figure 2b). These standards have been developed for fiber-reinforced polymer matrix composites and they are based on the principles of Linear Elastic Fracture Mechanics (LEFM). The present characterization effort is inspired by the guidelines recommended by these ASTM standards, but it uses additional experimental and analysis techniques to investigate the fracture properties of FM-300M adhesive and to account for its nonlinear response and fracture.

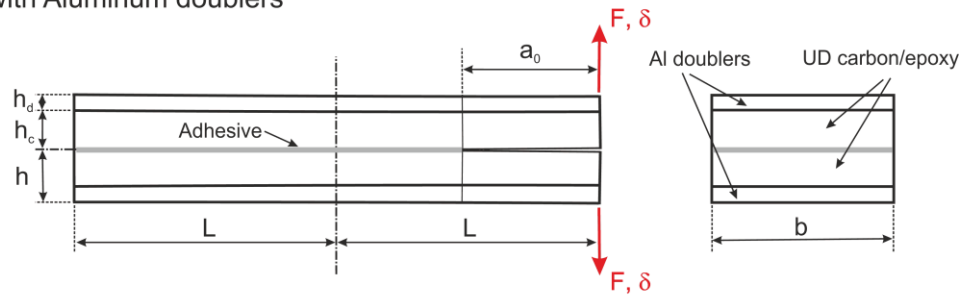
The characterization specimens were composed of two unidirectional (UD) TE-1 carbon/epoxy laminates of equal thickness bonded together with FM-300M adhesive. An initial crack was induced in the plane of the adhesive by inserting three layers of thin Teflon tape, which have combined thickness that is approximately equal to the thickness of the adhesive. For each case, the specimen configuration was designed to cause stable delamination propagation in the adhesive layer. Nine DCB, eleven ENF and ten MMB specimens were tested. The MMB specimens were tested at different mixed-mode ratios,  $B$ : 25%, 50%, 60% and 75%. The relevant material properties and dimensions of the characterization specimens,

including the half-length  $L$ , width  $b$ , initial crack length  $a_0$ , composite thickness  $h$ , adhesive thickness  $t_{adh}$ , and the MMB lever arm length  $c$  are shown in Table 4, with further details provided by Girolamo [14].

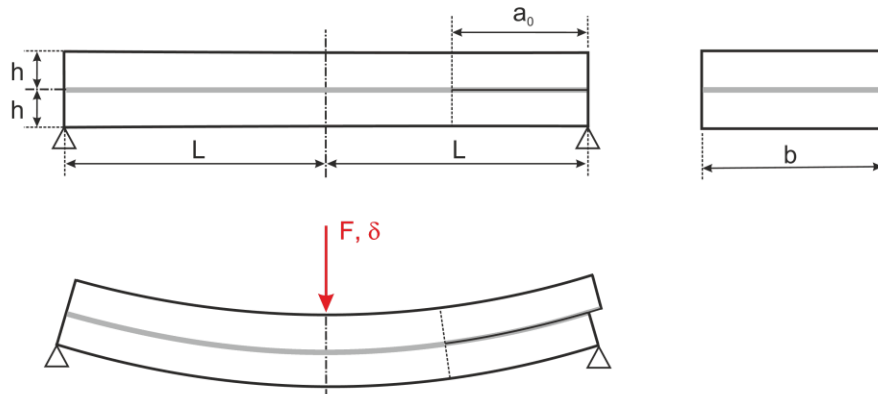
Table 4. Adhesive characterization specimen dimensions and material properties.

<b>DCB with doublers, dimensions [in.]</b>						
$h_{doubler}$	$h_{comp}$	$L$	$b$	$a_0$	$t_{adh}$	
0.063	0.060	3.94	0.98	0.886	0.010	
<b>ENF, dimensions [in.]</b>						
$h$	$L$	$b$	$a_0$	$t_{adh}$		
0.098	4.035	0.984	2.17	0.010		
<b>MMB, dimensions [in.]</b>						
	$h$	$L$	$b$	$a_0$	$c$	$t_{adh}$
MMB 0.24	0.061	2.76	0.992	1.18	4.49	0.010
MMB 0.48	0.061	2.76	0.992	1.18	2.36	0.010
MMB 0.57	0.098	3.86	0.984	1.81	2.87	0.010
MMB 0.74	0.098	3.94	0.984	1.81	2.32	0.010
<b>FM-300M Adhesive, material properties</b>						
$E$ [ksi] <sup>1</sup>		Poisson Ratio <sup>1</sup>		Thickness [in.] <sup>2</sup>		
456.		0.38		0.005		
<b>Aluminum 2024-T3, material properties</b>						
$E$ [ksi]	Poisson Ratio		Yield Str. [ksi]		Shear Str. [ksi]	
10600	0.33		50.		41.	
<sup>1</sup> Breitzman [15]		<sup>2</sup> Manufacturer datasheet				

(a) DCB with Aluminum doublers



(b) ENF



(c) MMB

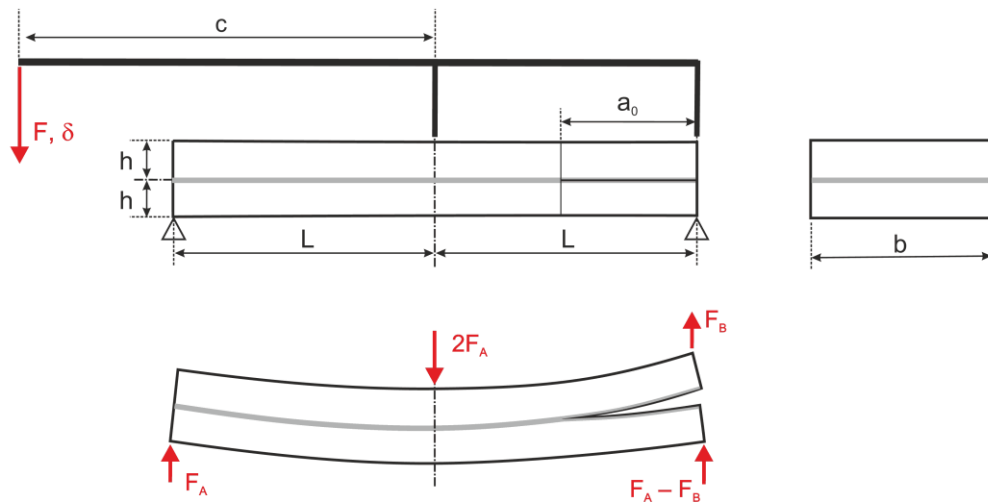


Figure 2. Schematics of the material characterization specimens: (a) Double Cantilever Beam (DCB), (b) End Notched Flexure (ENF), and (c) Mixed-Mode Bending (MMB) tests.

The experimental load-displacement curves for the DCB, ENF and MMB specimens are shown as black lines in Figure 3. The results of two different ENF tests are shown as will be explained later in this section. The experimental results for all specimens are shown together with their corresponding analytical solutions [16] shown in dashed lines. These analytical solutions were obtained by adjusting the fracture toughness for a best match with the steady-state propagation part of the experimental load-displacement curves (e.g., Figure 3a) [17]. It can be observed that some of the MMB and DCB specimens exhibit a load drop that is unlike the gradual load reduction represented by the analytical models. This sudden load drop was caused by the formation in some specimens of a delamination in the composite. This situation, which is referred to herein as a double delamination, is examined later in Section 4.3.5. In the case of double delamination, the propagation of damage in the adhesive is interrupted, so an exact value of the CERR for the adhesive is difficult to determine.

Experimental results show that the fracture toughness (CERR) is a function of the mode mixity. The toughness typically increases monotonically from the mode I fracture toughness  $G_{Ic}$  to the mode II fracture toughness  $G_{IIc}$ . Several empirical models have been proposed to describe this function. Herein, the mixed-mode fracture toughness  $G_c$  is described using the Benzeggagh-Kenane (B-K) criterion [18]:

$$G_c = G_{Ic} + (G_{IIc} - G_{Ic})B^\eta \quad \text{where } B = \left( \frac{G_{II}}{G_I + G_{II}} \right) \quad (1)$$

where the variable  $B$  is the mode mixity, and the exponent  $\eta$  is a curve-fitting parameter that is obtained from experiments with different mode mixities. The variables  $G_I$  and  $G_{II}$  are the energy release rates (ERR) in mode I and mode II.

The results of the fracture toughnesses obtained experimentally can be combined into a B-K mode mixity plot such as shown in Figure 4. In this graph, the mode mixity  $B$  for each data point is obtained from the assumptions made in the ASTM standards. The fracture toughnesses are obtained by the best fit of the analytical solutions to the corresponding force-displacement results, as explained above. The value of the B-K exponent that gives the best fit of the experimental data, represented by the red curve in Figure 4, is  $\eta = 1.7$ . It can be observed that this B-K fit of the test data is not particularly good. The function overestimates the toughness of the MMB results with low mode mixities, and it underestimates the toughness of the MMB tests with higher mode mixities. It appears that a better fit would have been obtained with a function that allows an inflection point at a mode mixity of about 60%, something that the B-K criterion cannot represent.

A detailed examination of the fracture processes in the ENF tests revealed that the assumption that adhesive undergoes pure shearing displacements is invalid. By performing observations with a microscope, it was found that  $45^\circ$  cracks develop in the adhesive and that the ligaments formed by these cracks tend to rotate and cause an opening displacement. The effect of this rotation of the ligaments is that the expected mode II toughness is not achieved.

A modified ENF test was conducted by applying constraints that prevent the mode I opening of the cracks. The result of this test is shown as ‘‘Clamped ENF’’ in Figure 3b. It was found that the toughness of the clamped ENF tests is 30% higher than without the clamps.

A B-K fit of the test data using the data from the clamped ENF with  $\eta = 2.3$  is shown in purple in Figure 4. This new fit of the test data offers a better approximation of the experimental points and is more representative of the mode mixities present in CSJ and DRJ joints.

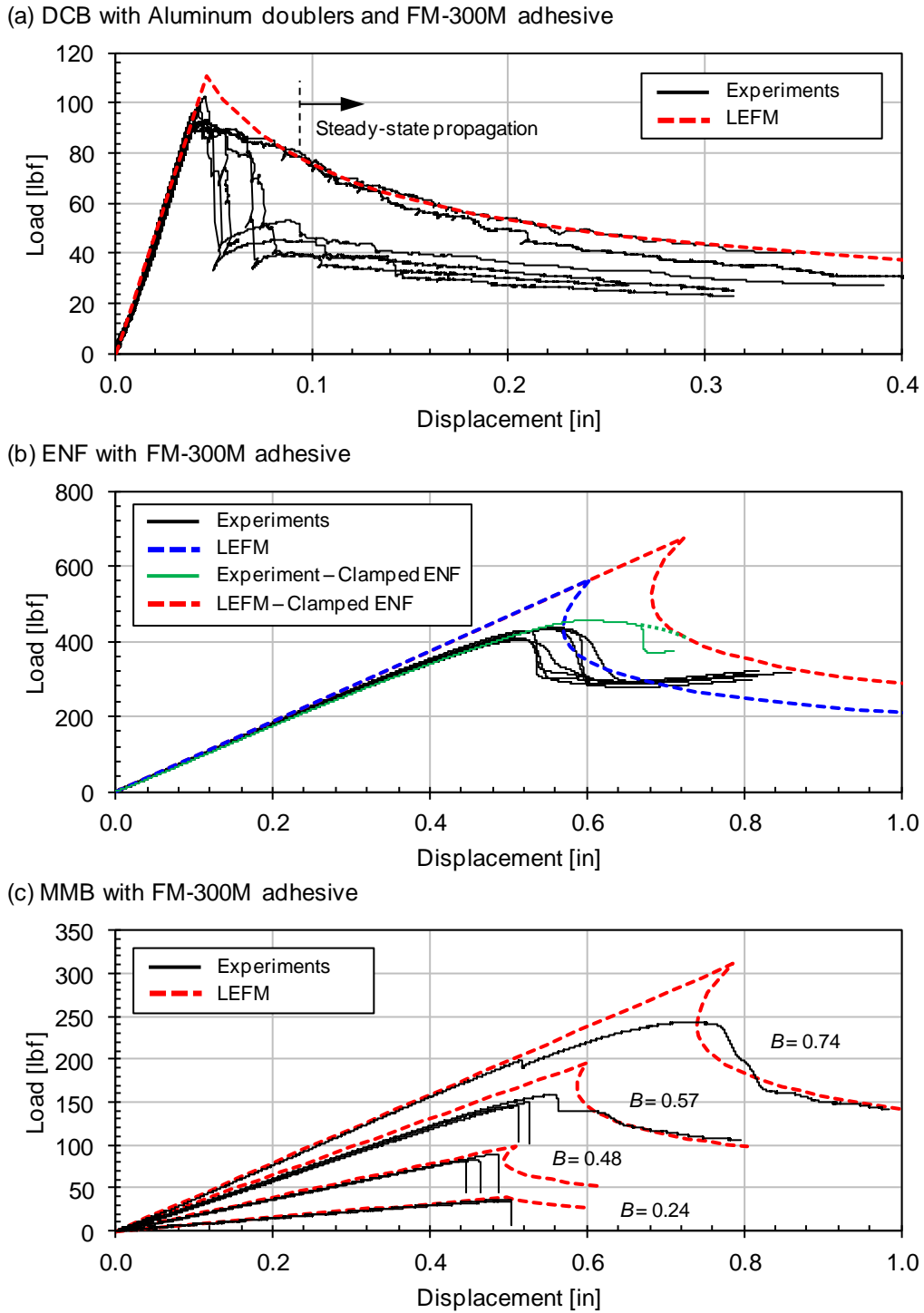


Figure 3. Experimental and analytical solutions for (a) the DCB tests, (b) the ENF tests, and (c) the MMB tests.

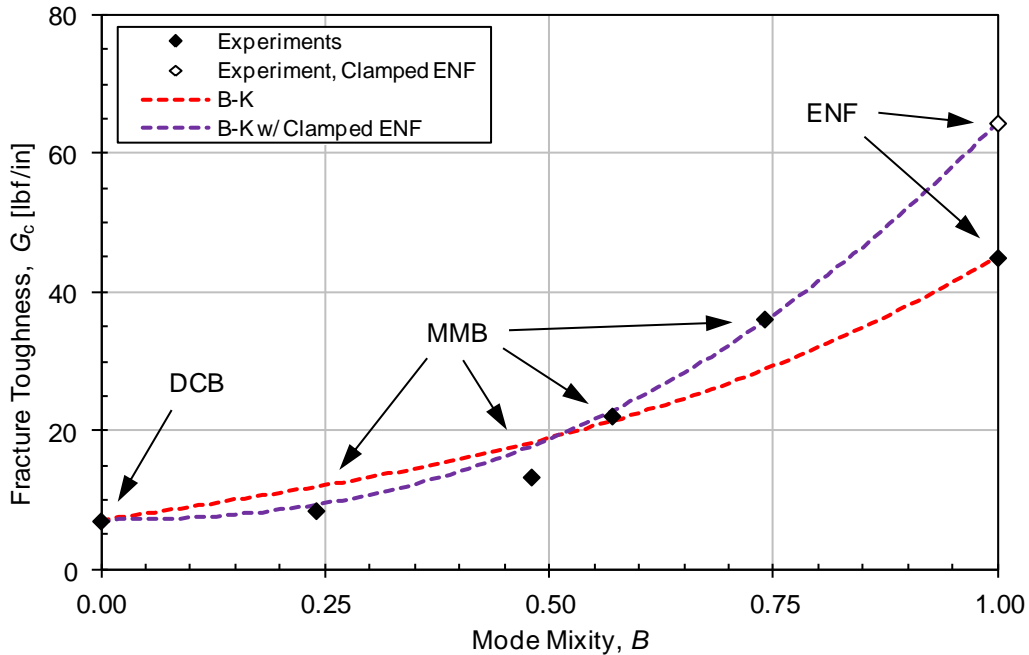


Figure 4. B-K criterion for FM-300M adhesive fracture toughness data.

#### 4.3.2 Cohesive Laws for Adhesive

The J-integral is an analysis technique that is used to calculate the fracture energy in problems for which the assumptions of LEFM do not hold. Nonlinear Fracture Mechanics (NLFM) is necessary when the volume of material subjected to irreversible nonlinearities, or the fracture process zone (FPZ), is not negligibly small compared to the structural dimensions, and must be taken into account. The J-integral consists of a contour integral whose value is equal the ERR, or work per fracture area, in a body that contains a crack. Rice [19] showed that the J-integral has three main properties:

1. It is path independent, i.e., integration along any closed contour surrounding the process zone gives the same result;
2. Its value is equal to the energy released in the process of damaging a nonlinear elastic body; and
3. Its derivative with respect to the displacement-jump at the crack tip is equal to the cohesive law.

The first property of the J-integral allows the selection of the most convenient path along which to integrate the stresses and evaluate the integral. The second property allows for the determination of the ERR from the tests, and the third property is used to extract the cohesive law that will be used in the cohesive elements by derivation of the experimental value of the J-integral with respect to the displacement-jump. A closed solution of the J-integral for the MMB test has not yet been found, therefore the current work focuses on the experimental estimation of the J-integral for the DCB and ENF tests.

A number of closed-form expressions for the J-integral have been developed based on analytical models of beams on inelastic foundations. Leffler [20] proposed the following solution for the mode II ENF specimen:

$$J_{ENF} \approx \frac{9}{16} \frac{F^2 a_0^2}{EW^2H^3} + \frac{3}{8} \frac{F\delta_t}{WH} \quad (2)$$

where  $E$  is the Young's modulus of the adherends in the fiber direction,  $H$  is the thickness of each arm,  $W$  is the width of the specimen,  $a_0$  is the initial crack length,  $\delta_t$  is the displacement-jump in the shear direction, and  $F$  is the applied load.

A closed form solution for the J-integral for the DCB test is provided by Högberg et al. [21]:

$$J_{DCB} = \frac{12}{EH} \left( \frac{F a_0}{WH} \right)^2 + 2 \frac{F}{W} \theta \quad (3)$$

where  $\theta$  represents the rotation of each arm at the crack tip. The values of the J-integrals for mode II and mode I, given by equations (2) and (3), can be determined experimentally by measuring the displacement jump  $\delta_t$  and the arm rotation  $\theta$ . These displacements and rotations are measured using a stereoscopic digital image correlation (DIC) system known as VIC-3D<sup>®</sup>.

A VIC-3D system was used to measure the displacement fields on the profile of the specimens near the crack tips during the tests. Figure 5 shows contour plots of the displacements on the edge of an ENF specimen before loading (Figure 5a) and at the instant prior to total separation (Figure 5b). The displacement is interrogated along the red vertical lines that are drawn at the crack tip. After removal of the rigid body rotations, the horizontal displacements as a function of the through-thickness position have the distribution shown in Figure 5c. In this plot, the desired displacement jump  $\delta_t$  is the distance between the two vertical lines. This process is performed for all the images from the initial stage to the total separation point, and for each image the displacement jump is associated to the corresponding applied load,  $F$ . By substituting the displacement jumps into equation (2), the J-integral result shown in Figure 5d is obtained. Finally, the cohesive law for mode II is obtained by taking the derivative of the J-integral with respect to the displacement jump. The resulting cohesive laws for three ENF specimens are shown in Figure 5e.

A similar procedure is followed for the DCB specimens. The displacements from which the rotations of the composite arms are calculated are shown in Figure 6a. The deformed configuration of the DCB specimen just before the total separation of the adhesive interface is shown in Figure 6b. The rotation of the composite arms is highlighted by the relative displacements of four points representing the normal directions of the two arms. The J-integral obtained using equation (3) for three DCB specimens are shown in Figure 6c. The resulting mode I cohesive traction-separation law is shown in Figure 6d.

It should be pointed out that, by definition, the area under a cohesive curve corresponds to the maximum value of its J-integral, and that this value is the CERRs for the adhesive material:  $J_{I \max} = G_{Ic} \cong 7.14$  lbf/in and  $J_{II \max} = G_{IIc} \cong 45.1$  lbf/in. The maximum values of the cohesive curves correspond to the strengths of the adhesive. The resulting strengths for modes I and II are approximately 11.6 and 6.7 ksi, respectively. These strength values are in good agreement with the von Mises criterion, which requires  $\frac{\sigma_I}{\sigma_{II}} = \sqrt{3}$ , and are also comparable to the experimental observations of Breitzman et al. [15].

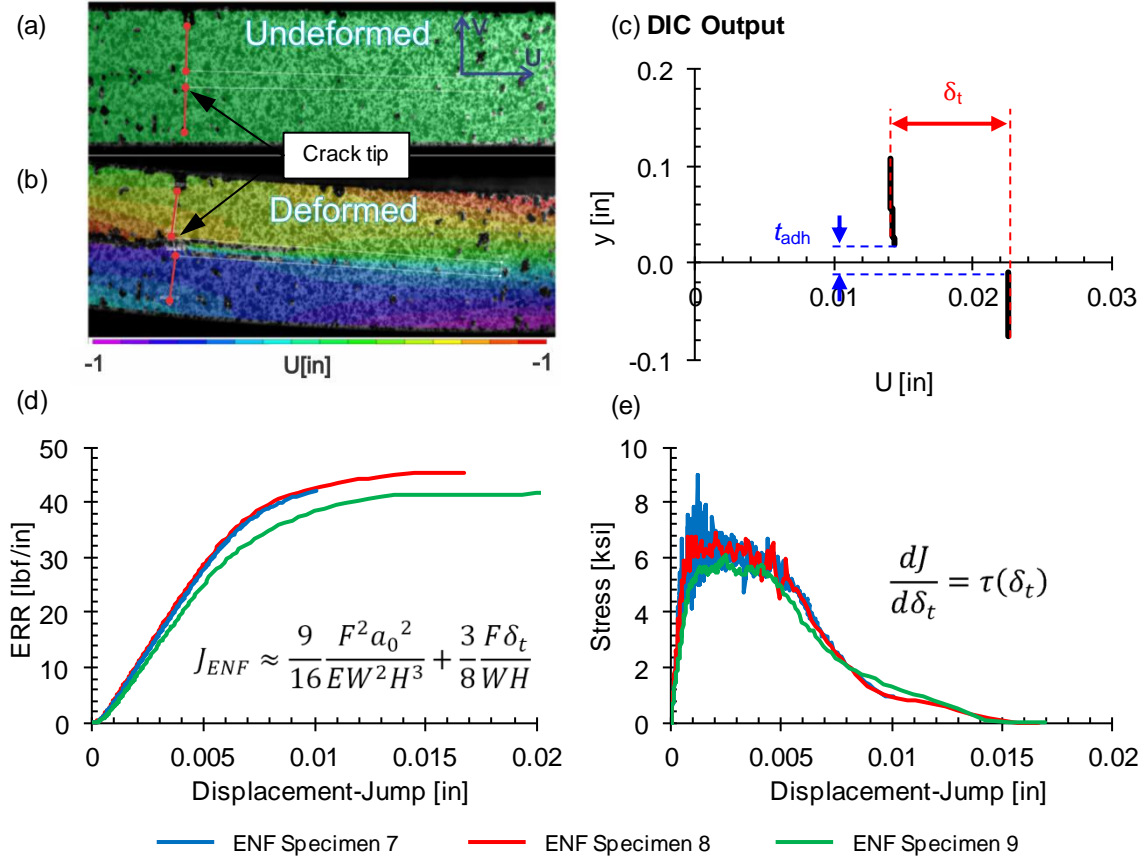


Figure 5. Procedure to estimate the Mode II cohesive law: (a) displacement field around the crack tip without external load; (b) displacement field around the crack tip at maximum load; (c) output from the interrogation of the vertical line through the crack tip; (d) J-integral vs. displacement-jump; and (e) the experimental cohesive law.

It can be observed that the mode I and mode II cohesive laws exhibit different material responses at different stages of their deformation histories:

1. The first part of each law is a linear/elastic section in which the curve can be approximated by a straight line. For mode I, the slope is  $K_I \cong 44,200 \text{ kip/in}^3$ , and for mode II  $K_{II} \cong 14,700 \text{ kip/in}^3$ . The Young's modulus of the adhesive is thus  $E = t K_I = 0.01 \text{ in} \times 44,200 \text{ kip/in}^3 \cong 442 \text{ ksi}$ . The shear modulus is  $G = t K_{II} = 0.01 \text{ in} \times 14,700 \text{ kip/in}^3 \cong 147 \text{ ksi}$ , so these moduli satisfy the expression  $E = 2G(1 + \nu)$ . The moduli also correlate well with the corresponding values of 450 and 160 ksi measured by Breitzman et al. [15].
2. The mode II cohesive law includes a second part consisting of a nonlinear/plastic section in which the local tangent of the curve is almost horizontal.
3. The final part of each law is a softening section of decreasing tractions along which the material is increasingly unable to withstand the applied tractions.

Curve-fit approximations of the experimental mode I and mode II cohesive laws could be tabulated for use as inputs to cohesive models. However, there are no procedures for establishing mixed-mode cohesive

laws from tabulated mode I and mode II data. On the other hand, mixed-mode models for bilinear cohesive are well established. To take advantage of the available bilinear models, the experimental cohesive laws were approximated by superposing two bilinear curves, referred to as Law A and Law B in Figure 7. Therefore, the mode I response is represented by the sum of the bilinear laws I-A and I-B, and the mode II response is represented by the sum of laws II-A and II-B. The bilinear laws of Figure 7 are defined through the parameters listed in Table 5. For mixed-mode cases,  $\eta$  values of 2.6 and 2.2 were used in the B-K criterion for laws A and B, respectively.

The shape of the cohesive law of the clamped ENF specimen was not determined using the outlined J-integral approach. Instead, the difference between the standard and clamped ENF results, in terms of fracture toughness, was simply added to Law B-II, extending the “tail” of the mode II cohesive law. The amount of fracture toughness added to Law II-B was obtained by comparing the CERR determined for the standard ENF specimens using the J-integral approach and the CERR estimated by comparing the LEFM solution and the clamped ENF load-displacement results. As a result, the total fracture toughness of Law B-II was increased from 22.3 to 44.5 lbf/in.

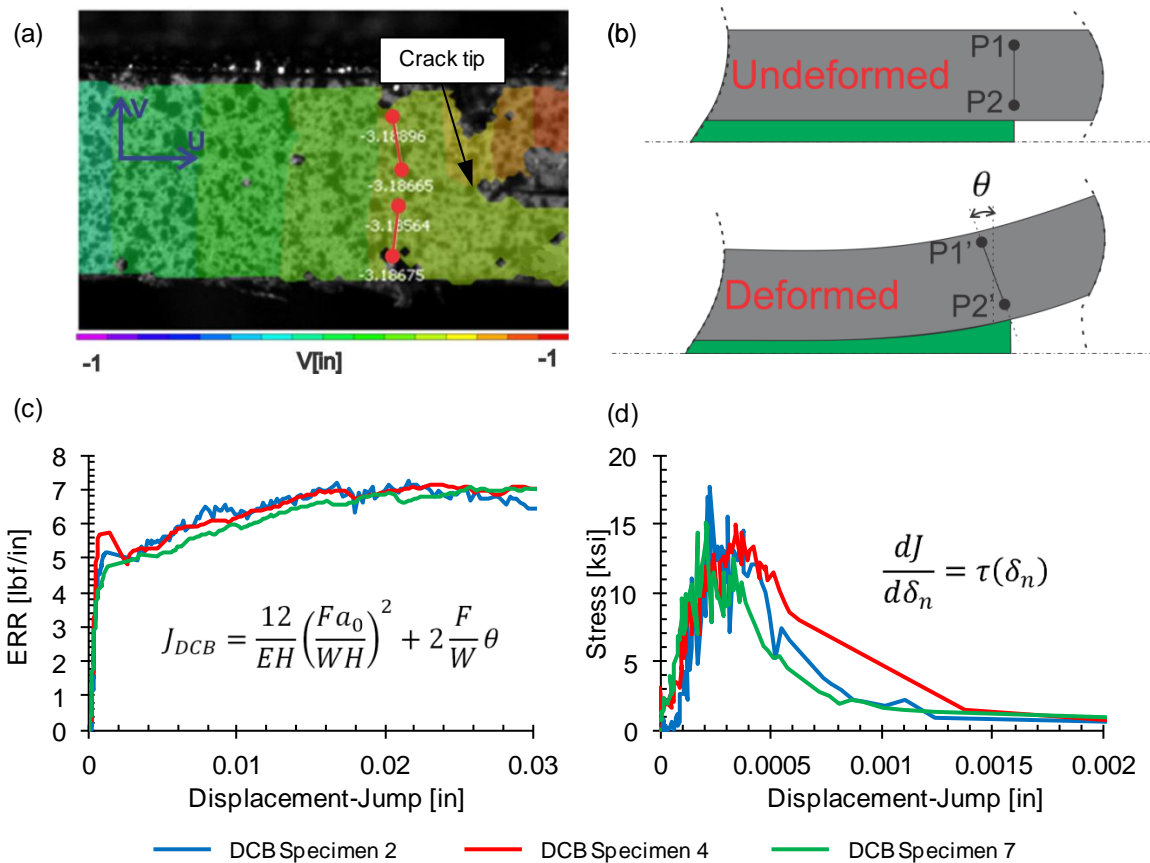


Figure 6. Procedure to estimate the Mode I cohesive law: (a) interrogation points along the vertical line through the crack tip; (b) rotation of the composite arm; (c) J-integral vs. displacement-jump; and (d) the experimental cohesive law.

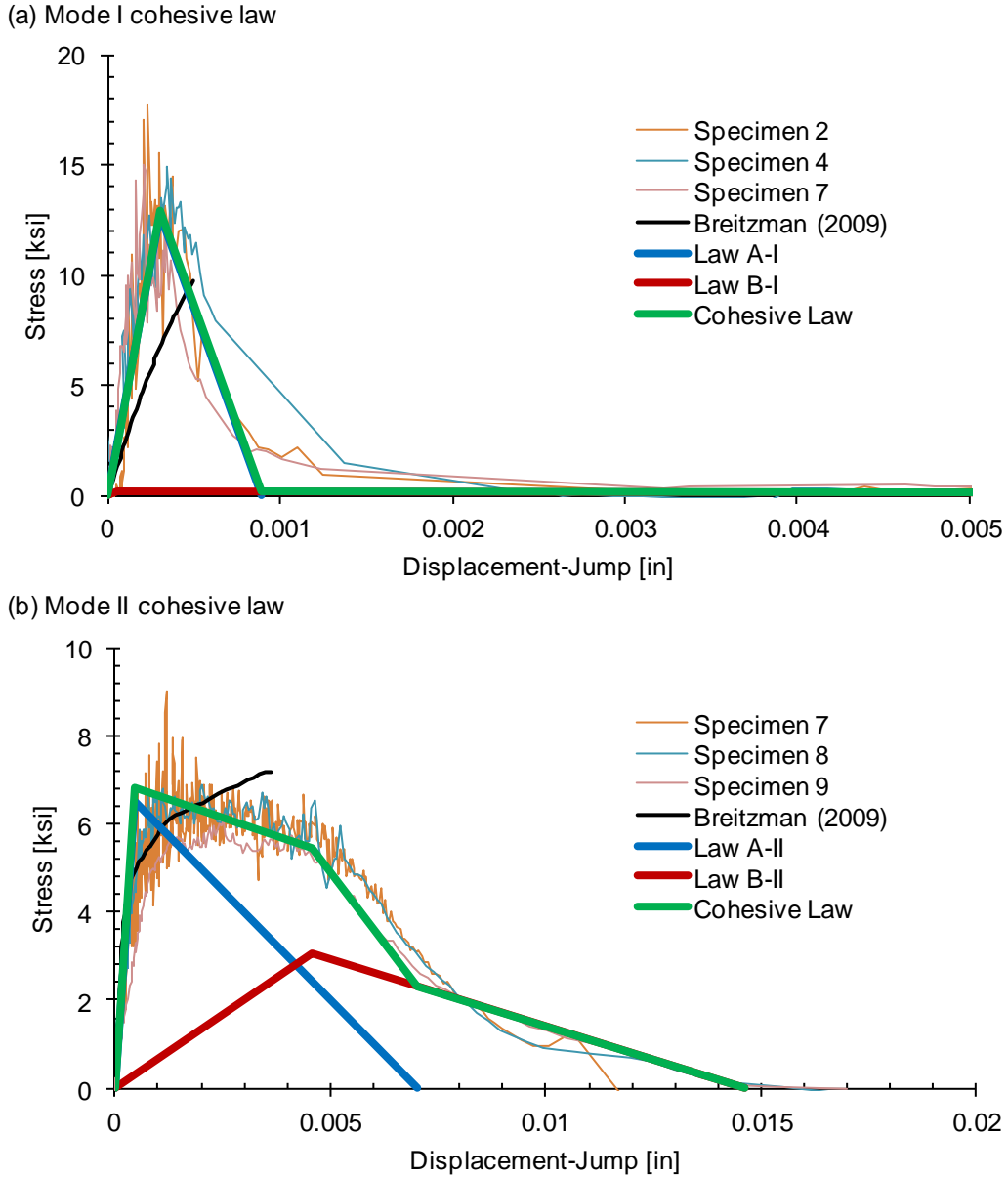


Figure 7. Measured cohesive laws and their approximation by superposition of bilinear laws for (a) Mode I and (b) Mode II.

Table 5. FM-300M material properties based on the experimental DCB and ENF test specimens.

Elastic Properties		Strength Properties		Fracture Properties	
$K_{I-A}$	42400 kip/in <sup>3</sup>	$\sigma_{I-A}$	12.8 ksi	$G_{Ic-A}$	5.71 lbf/in
$K_{II-A}$	14700 kip/in <sup>3</sup>	$\sigma_{II-A}$	6.53 ksi	$G_{IIc-A}$	22.8 lbf/in
$K_{I-B}$	3700 kip/in <sup>3</sup>	$\sigma_{I-B}$	0.18 ksi	$G_{Ic-B}$	1.43 lbf/in
$K_{II-B}$	660 kip/in <sup>3</sup>	$\sigma_{II-B}$	3.05 ksi	$G_{IIc-B}$	22.3 lbf/in
				$\eta_A$	2.6
				$\eta_B$	2.2

### 4.3.3 Adhesive Material Properties for the Composite Joint Models

One of the most challenging aspects in the development of a mixed-mode cohesive element is that the instantaneous mode mixity must be evaluated using nodal displacements. In problems such as the MMB, where bending induces cracks to grow under mixed mode, damage at any point along the crack path always initiates in a predominantly mode II condition, and the mixity evolves towards a predominantly mode I condition before complete failure. A well-formulated cohesive element must be capable of predicting this instantaneous local change in mode mixity as well as being able to predict the correct average value at failure. This average, or global mode mixity, must also tend toward the one predicted by LEFM when the length of the process zone tends to smaller values. The Turon cohesive model [22] used in the present characterization of the adhesive has been shown to be able to predict the correct local and global mode mixity provided that the following constraint is met:

$$\frac{K_{II}}{K_I} = \frac{G_{Ic}}{G_{IIc}} \left( \frac{\sigma_{II}}{\sigma_I} \right)^2 \quad (4)$$

Equation (4) imposes a constraint relating the cohesive stiffnesses, strengths, and toughnesses in modes I and II, thereby decreasing the freedom with which these material properties can be selected to best approximate the experimentally observed nonlinear behavior. In fact, this constraint may conflict with some experimental observations. For instance, if an adhesive's Poisson ratio is  $\nu = 0.5$ , then  $K_I = 2(1 + \nu)K_{II} = 3K_{II}$ . If the material fails according to the von Mises criterion, then  $(\sigma_I)^2 = 3(\sigma_{II})^2$ . Therefore, equation (4) imposes  $G_{Ic} = G_{IIc}$ , which is usually incorrect. Nevertheless, equation (4) represents a condition necessary for the Turon model and, in the absence of a more general mixed-mode cohesive model, the experimental data was adjusted to comply with this artificial constraint. It should be noted that for zero-thickness cohesive elements, the penalty stiffness terms do not represent the physical stiffness of the material, and the requirement to define them according to the strength and fracture toughness properties does not affect the overall performance of the model.

Although equation (4) was derived for the Turon model, it was also found by numerical experimentation that this constraint is also necessary in the Abaqus COH cohesive elements [23]. Parametric studies have shown that when equation (4) is satisfied, the predictions of crack propagation obtained with the Turon UEL and with the Abaqus COH elements are in close agreement.

In the superposition proposed to represent the response of the FM-300M adhesive, both Law A and B used in the superposition must satisfy the Turon constraint. As a result, it was necessary to find approximations to the mode I and mode II cohesive laws that satisfy the conditions imposed by equation (4). It was assumed that the finite element predictions would be least sensitive to changes to the adhesive stiffnesses, and so the majority of the error introduced to the computational material property set was associated with the stiffness terms.

The material properties used in the modeling of the joint specimens that satisfy Turon's constraints and that use the pure mode II properties measured from the clamped ENF test are listed in Table 6. With this full set of adhesive fracture properties defined, it was then possible to develop finite element models of the adhesive characterization specimens.

Table 6. FM-300M material properties for use in the bonded joint finite element models.

Elastic Properties			Strength Properties			Fracture Properties		
$K_{I-A}$	87763	kip/in <sup>3</sup>	$\sigma_{I-A}$	10.3	ksi	$G_{Ic-A}$	4.00	lbf/in
$K_{II-A}$	7368	kip/in <sup>3</sup>	$\sigma_{II-A}$	6.67	ksi	$G_{IIc-A}$	20.0	lbf/in
$K_{I-B}$	1636	kip/in <sup>3</sup>	$\sigma_{I-B}$	1.31	ksi	$G_{Ic-B}$	3.14	lbf/in
$K_{II-B}$	738	kip/in <sup>3</sup>	$\sigma_{II-B}$	3.19	ksi	$G_{IIc-B}$	44.5	lbf/in
						$\eta_A$	2.6	
						$\eta_B$	2.2	

#### 4.3.4 Finite Element Models of Characterization Specimens

Two-dimensional parametric finite element models of the characterization specimens were created for the commercial finite element program Abaqus/Std 6.10-1 [23], which uses an implicit solution procedure. Although implicit schemes tend to have convergence difficulties in problems with material softening, all settings related to viscous damping and viscoelastic regularization, which are usually used to improve the convergence rate of the iterative procedure, were set equal to zero to ensure that the models dissipate the correct amount of fracture energy. The models were composed of plain strain CPE4 elements for the carbon/epoxy plies and two superposed layers of COH2D4 cohesive elements for the adhesive laws A and B.

The models are composed of three sections, as shown in Figure 8. Section AB corresponds to the initial crack; section BC has a refined mesh for accurate prediction of crack propagation, and section CD, which is coarser and where crack propagation is not considered. The number of elements in the horizontal direction in the section BC was chosen such that the elements are smaller than one third of the length of process zone of either bilinear law A or B. In section BC, the element size in the length direction is approximately 0.02 inch. Five elements through the thickness of each arm are sufficient to maintain an aspect ratio of less than 2.5 throughout the model. The same model was used for the DCB, ENF and MMB specimens by changing the dimensions and boundary conditions as required.

The model results for each of the characterization specimen configurations using the material properties listed in Table 6 correlated well with the experimental load-displacement results, as can be seen in Figure 9. However, simulations of the DCB and ENF models do not correlate as well with the experimental load-deflection data as simulations performed using the best-fit material properties (Table 5). Nevertheless, the adjusted values in Table 6 are preferable because they ensure that the mode mixity is properly calculated by the cohesive elements. The plotted MMB load-displacement curves have an adjustment to their displacement values to account for the compliance of the experimental test fixtures. Test fixture compliances of 0.0003, 0.0004, 0.0008, and 0.0015 in/lbf were used for the MMB75, MMB60, MMB50, and MMB25 models, respectively.

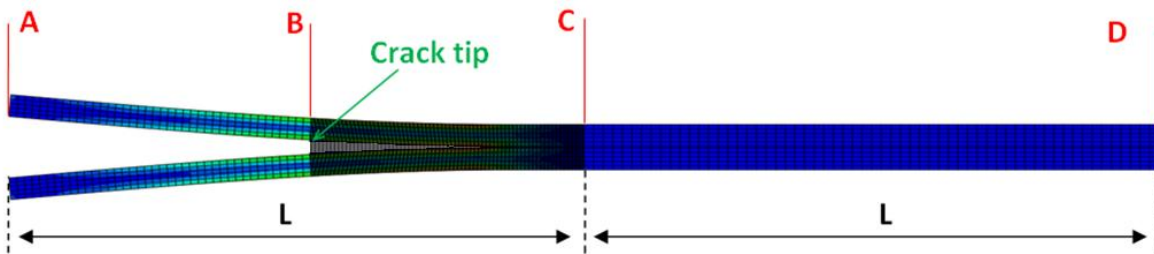


Figure 8. Mesh of the characterization specimen finite element models; DCB shown.

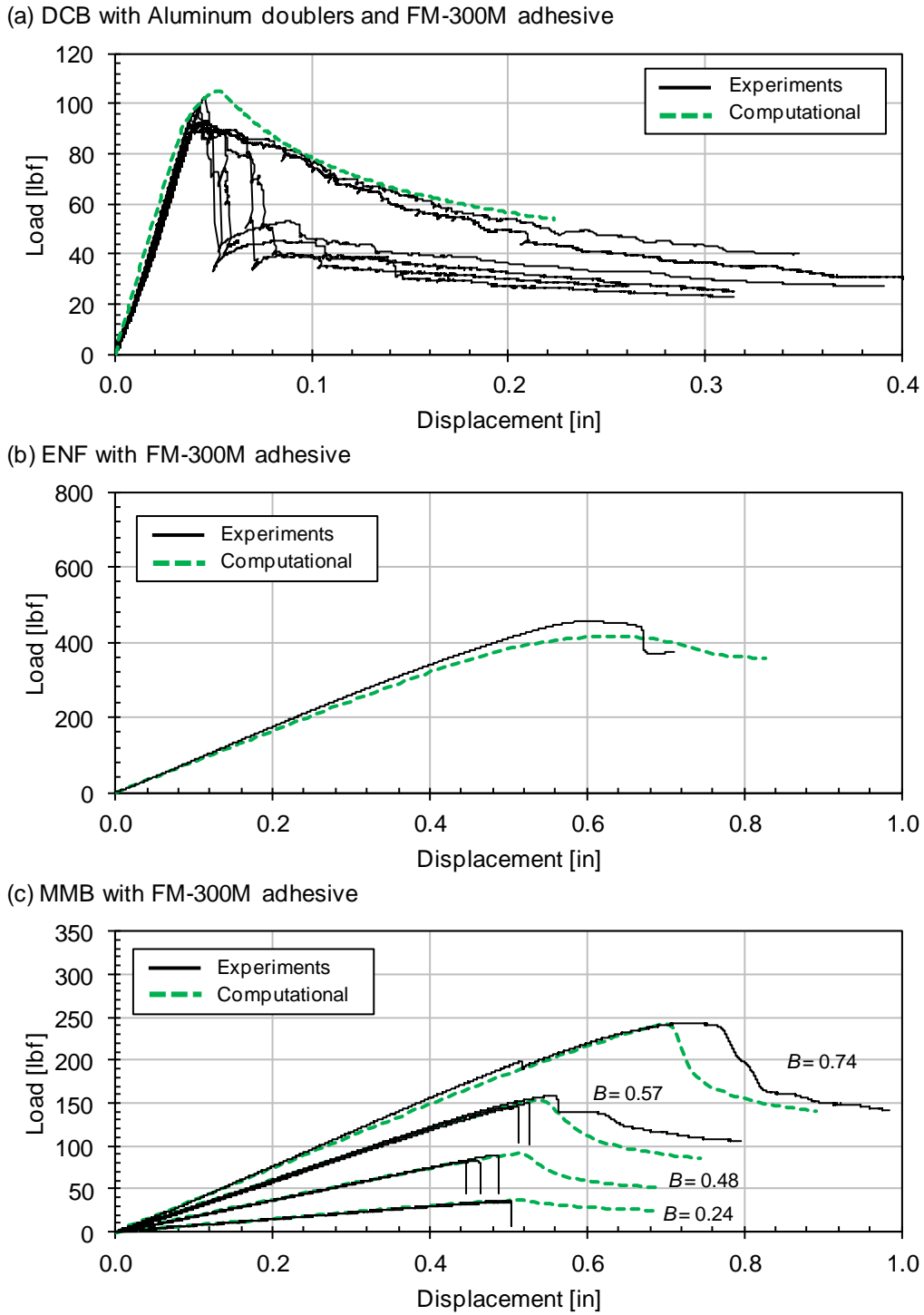


Figure 9. Experimental and computational results for (a) the DCB tests, (b) the clamped ENF test, and (c) the MMB tests using the material properties listed in Table 6.

### 4.3.5 Double Delamination

In the experimental section of this report, it was mentioned that some specimens exhibited a phenomenon referred to herein as a double delamination. In these specimens, consisting predominantly of DCB and low mode mixity MMB specimens, a secondary delamination parallel to the adhesive developed in the composite ply adjacent to the adhesive, as shown in Figure 10a. The fracture toughness for delamination being approximately five times lower than that of the adhesive, the delaminations, once initiated, grow unstably and prevent further damage development in the adhesive. In some specimens, a short period of stable delamination growth was observed. In these specimens, a thin bridge of  $0^\circ$  fibers could be observed between the delamination and the adhesive. In all specimens, a short amount of delamination propagation causes the bridge to stretch and then the fibers break. The delamination to the left of the break point closes, which initially confused the authors into thinking that the crack in the adhesive migrated into a different interface by propagating through a layer of fibers.

Since the instability in the delamination made the sequence of events difficult to interpret, this phenomenon was investigated using a three-dimensional model of the MMB specimen. The model is composed of 8-node C3D8 elements for the composite, a layer of superposed cohesive elements for the adhesive, and two zero-thickness layers of cohesive elements in planes above and below the adhesive layer for delamination. The distance between the adhesive and the cohesive layers was a model parameter that was investigated. The analyses indicate that, for certain combinations of peel and interlaminar shear strength that are effectively lower than those of the adhesive, a delamination can initiate in the  $0^\circ$  ply immediately above the adhesive layer. The threshold of the interlaminar strengths that allow this delamination to occur is higher when the distance between the cohesive plane and the adhesive is smallest.

Finally, the analyses predict that the load-displacement fracture of specimens with double delamination is much more brittle than those in which the fracture was contained within the adhesive. The blue line in the force-displacement plot in Figure 11 corresponds to a model in which the fracture is contained within the adhesive, and the red line is for an identical model in which the interlaminar strengths were lowered by 10%. It can be observed that the response after failure of the second model is more similar to those of the three specimens than the model without composite delamination.

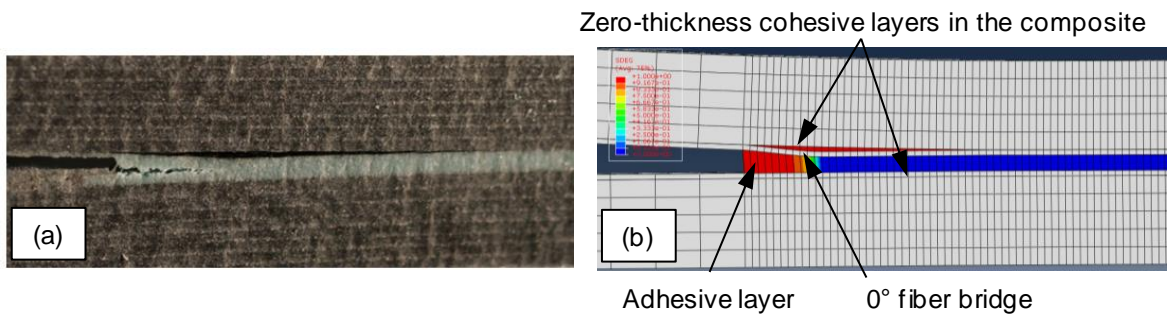


Figure 10. Double delamination in MMB 50%; a) experiment and b) 3D model.

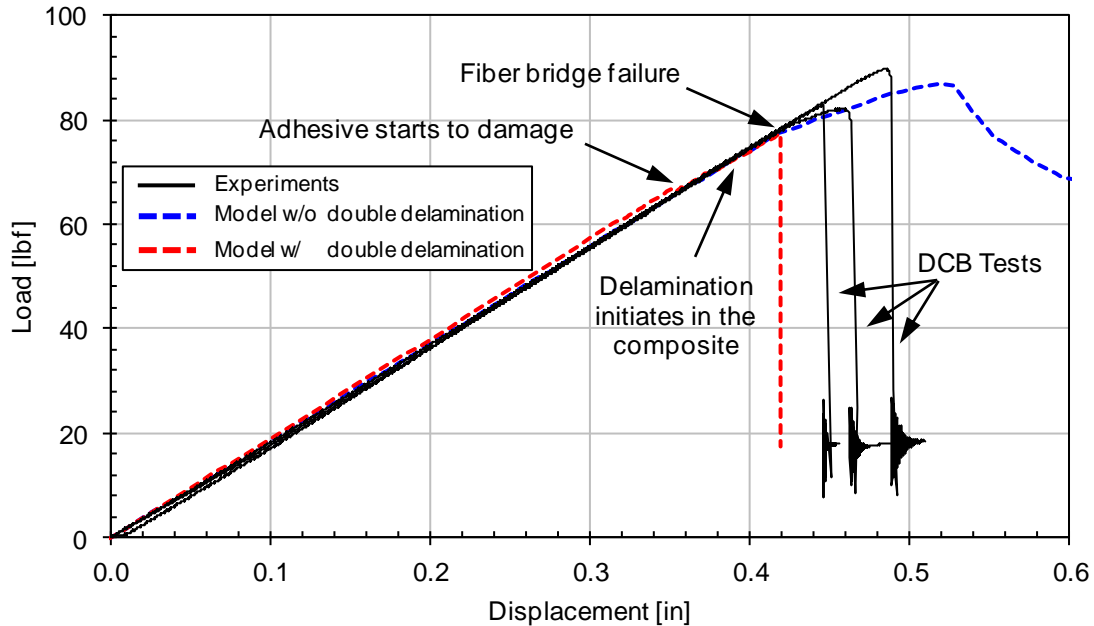


Figure 11. Load-displacement curves for the 50% MMB specimens that exhibited the double delamination failure mechanism — experimental and computational results.

## 5 Finite Element Models of Bonded Composite Joints

The progressive damage analysis finite element models of the joint specimens were solved using Abaqus 6.10-1. Custom user subroutines were used to define the constitutive responses of carbon/epoxy plies (via continuum damage mechanics) and the honeycomb core material. Due to the convergence difficulties associated with progressive damage and the softening of damaged material, the models were solved with Abaqus/Explicit in double precision. Elements were not removed from consideration after failing for either the CDM or cohesive damage methods.

The models were solved in two steps: one taking into account the thermal expansion, and a second for the application of the tensile or compressive loads. For computational efficiency, the time periods of the steps were selected to be as short as possible without inducing any significant dynamic forces. For the thermal steps, it was found that a time step of 0.005 second was sufficiently long. For the loading steps, it was found that a time step of 0.05 second represented the best compromise between computational efficiency and an approximation of a quasi-static solution. Loading rates were increased sinusoidally within each load step to reduce any applied accelerations and their corresponding model vibrations.

Variable mass scaling was used to decrease the solution time by increasing the minimum stable time increment to  $2.e-07$  second throughout the models (i.e., using less than 275,000 increments total, which is much less than the  $2.e+06$  increment limit recommended for double precision cases). The selection of this stable time increment, along with the material stiffnesses and element sizes used in the models, led to initial model-wide percent changes in mass to be on the order of 50 to 150 times. Mass scaling factors were updated every 500 solution increments to account for any local changes in elemental stiffness, gradually increasing the percent mass change as the solver proceeded.

## 5.1 Pristine Sandwich Panel

The pristine panel represents the composite component whose response and strength is used as a reference for comparison with the CSJ and DRJ joint concepts. Unlike the joints, the pristine panel is devoid of stress concentrations that would cause damage localization at any particular location within the specimen. Therefore, it is not necessary to model the full length of the pristine panel. Instead, a model of reduced dimensions was created. The models of the tensile and compressive pristine panel specimens represent a panel that is 1 inch long and 0.25 inch wide, as shown in Figure 12a. Symmetry is assumed through the center of the honeycomb core. The short edges of the model are constrained in the facesheet planar directions, with the long edges left free. In order to avoid premature failure near the boundary conditions, 0.125 inch of material from both constrained edges is modeled with elements with a linear-elastic constitutive response. Loads were applied uniformly by displacing one of the short model edges. With these assumptions, the predicted strengths are associated with the ideal response of the material, subjected to either a perfectly uniform extension or compression.

Each ply of the facesheet is represented with a single layer of solid three-dimensional reduced integration elements, C3D8R. Between each ply, a layer of zero-thickness COH3D8 cohesive elements is included. The approximate in-plane element size (i.e., edge length) for the solid and cohesive elements is 0.015 inch. The in-plane size of the honeycomb core mesh was selected to coincide with the core cell size. The much coarser mesh of the honeycomb core is connected to the underside of the facesheet mesh using tie constraints.

## 5.2 Conventional Splice Joint (CSJ)

The three-dimensional parametric conventional splice joint model shown in Figure 13a expands upon the model of the pristine sandwich model described in the previous section by adding a six-ply doubler to join two identical pristine panels. The model is defined parametrically so that the overall size of the splice, the length/presence of a Teflon insert, the thicknesses of the plies and the adhesive, the locations of the ply terminations, the length of the ply drops, and mesh densities throughout the model can be altered easily to incorporate minor design changes. Each ply in the sandwich facesheets in the splices is represented with a single layer of three-dimensional solid elements through-the-thickness. The in-plane element size in the facesheets and splices is equal to the ply thickness (i.e., 0.0075 inch). Layers of zero-thickness cohesive elements are located between all plies of different orientations.

The layer of adhesive between the facesheets and the splices is modeled using two coincident layers of finite-thickness, bilinear COH3D8 cohesive elements. The Teflon insert near the joint gap is represented by setting the strength and fracture toughness properties of the adhesive elements to extremely low values, causing them to fail very early in the analyses. As such, the elements representing the Teflon insert are able to carry compressive normal loads, but zero shear or tensile normal loads.

The honeycomb core is represented in the CSJ models by a layer of two-node T3D2 truss elements, initially oriented in the  $z$ -direction. As a result, the transverse shear stiffness of the honeycomb core is neglected. However, because there is no significant bending in the CSJ model, it was determined that neglecting the honeycomb core transverse shear stiffness does not have a significant effect on the analysis results.

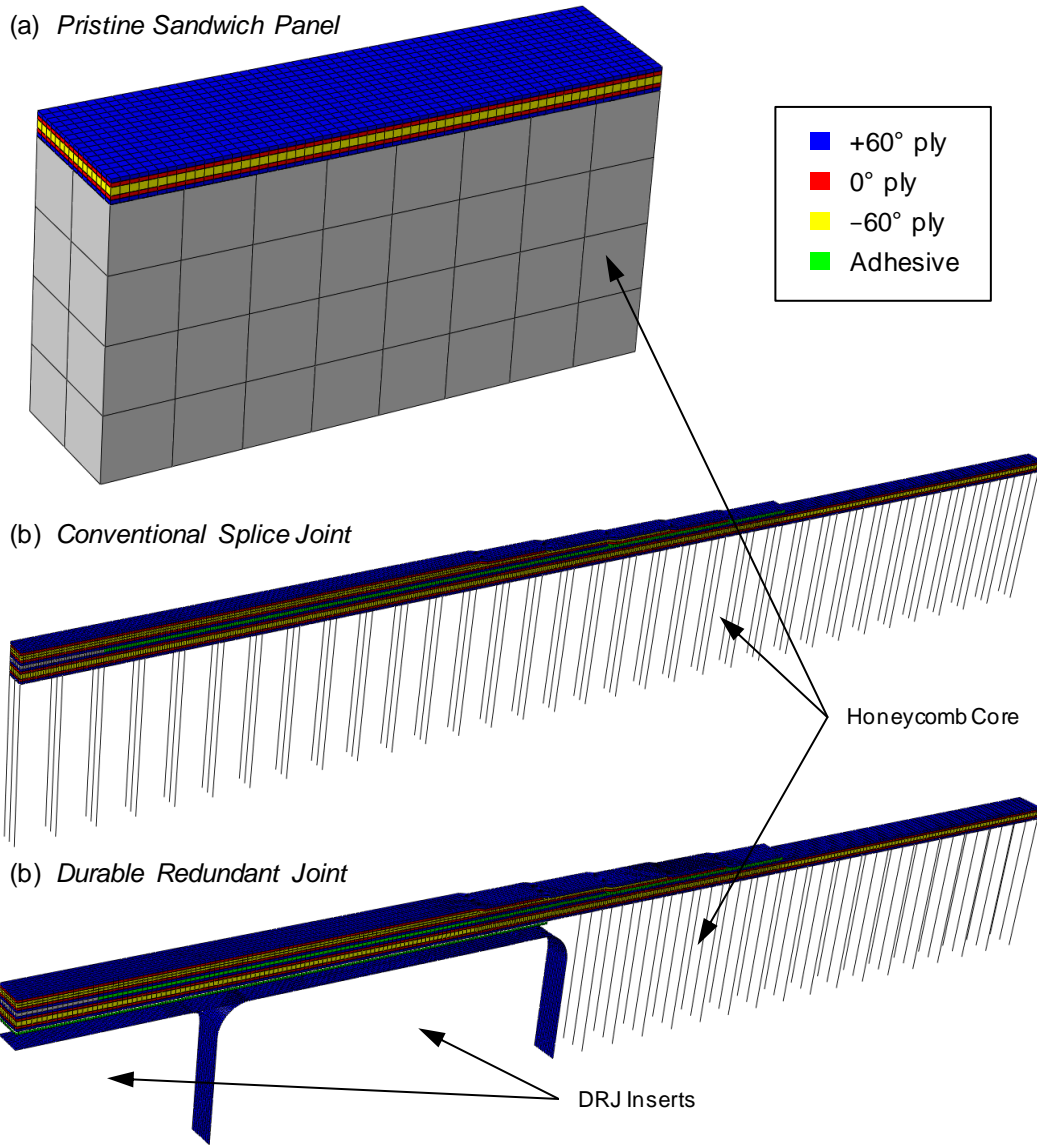


Figure 12. FE meshes for (a) the pristine sandwich panel, (b) the conventional splice joint, and (c) the durable redundant joint.

As in the case of the pristine panel models, the CSJ models are not intended to study the possible development of damage in the load introduction regions of the specimens. As a result, symmetry is assumed at the joint center ( $x = 0$  plane), and through the center of the honeycomb core ( $z = 0$  plane). In addition, only 4 inches along the length of the quarter specimen are modeled, assuming that a relatively uniform strain state is present at this distance from the joint center. For tensile loading cases, symmetry boundary conditions are applied along the splice plies at the joint center, leaving the facesheet nodes free, Figure 13b. For compressive loading cases, symmetry boundary conditions are applied for both the splice and facesheet nodes. Loads are applied by uniformly displacing the right side of the facesheet and honeycomb core in the positive or negative  $x$ -direction for tensile and compressive loading, respectively. In order to reduce the analysis times, the CSJ models were solved with a highly reduced width of 0.06 inches (i.e., 8 elements).

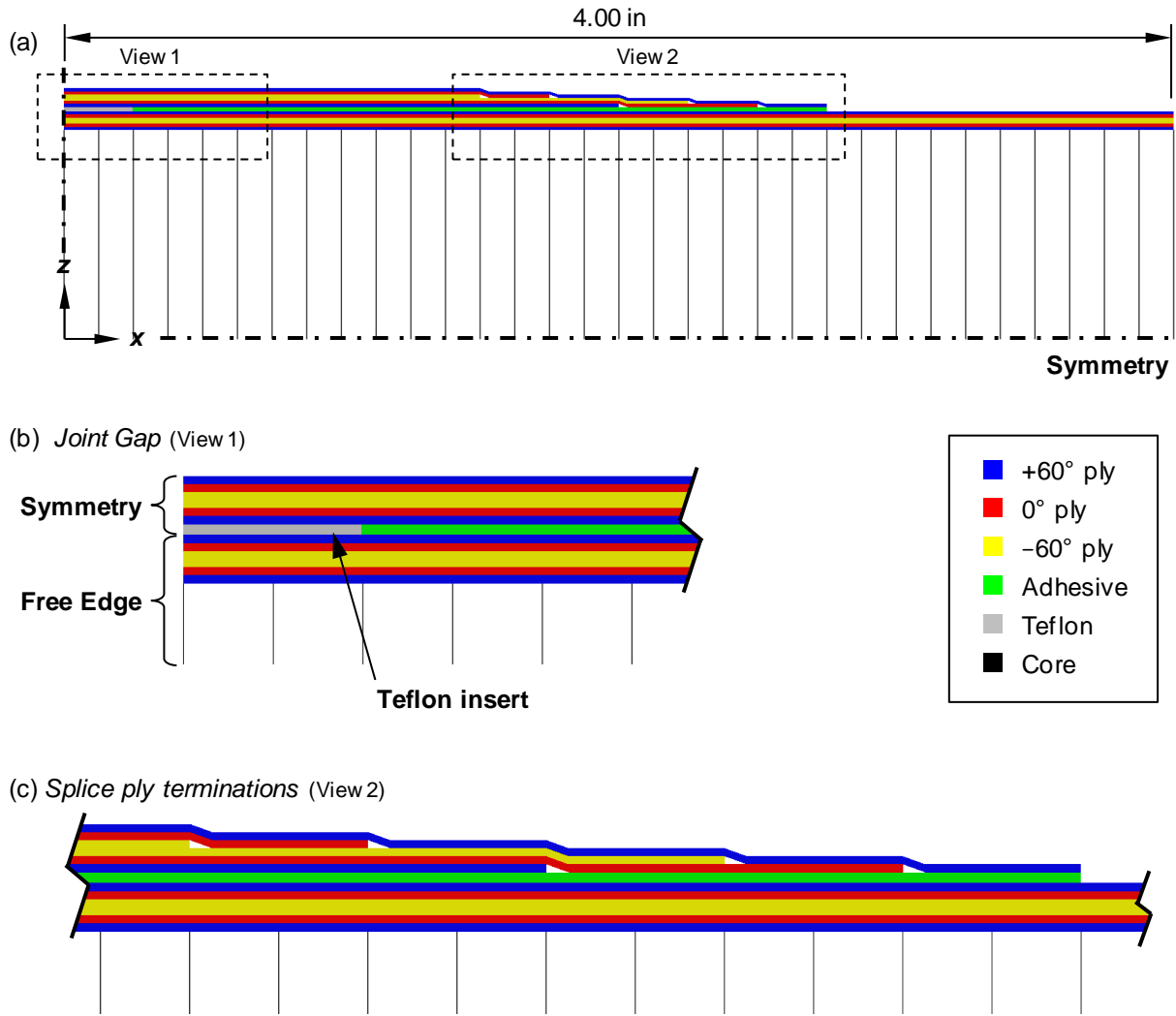


Figure 13. Cross-sectional view of the FE mesh for the conventional splice joint models.

### 5.3 Durable Redundant Joint (DRJ)

The DRJ model expands further on the parametric definition of the conventional splice joint model. As mentioned, the honeycomb sandwich and exterior doublers of the DRJ and CSJ specimens are identical, and, as a result, only the removal of the inner two inches of the honeycomb core truss elements from the CSJ model is required to accommodate the additional DRJ inserts, Figure 14a.

Due to the larger number of plies in the joint area relative to the pristine sandwich facesheets, it was assumed that no significant damage would develop in the DRJ inserts. As a result, the inserts are represented with S4R shell elements with linear elastic stiffness properties and are not capable of modeling damage. The layer of adhesive connecting the DRJ inserts to the interior surface of the facesheets is modeled with two layers of coincident bilinear cohesive elements. The shell elements representing the DRJ inserts are tied to the bottom surface of the cohesive elements that represent the adhesive.

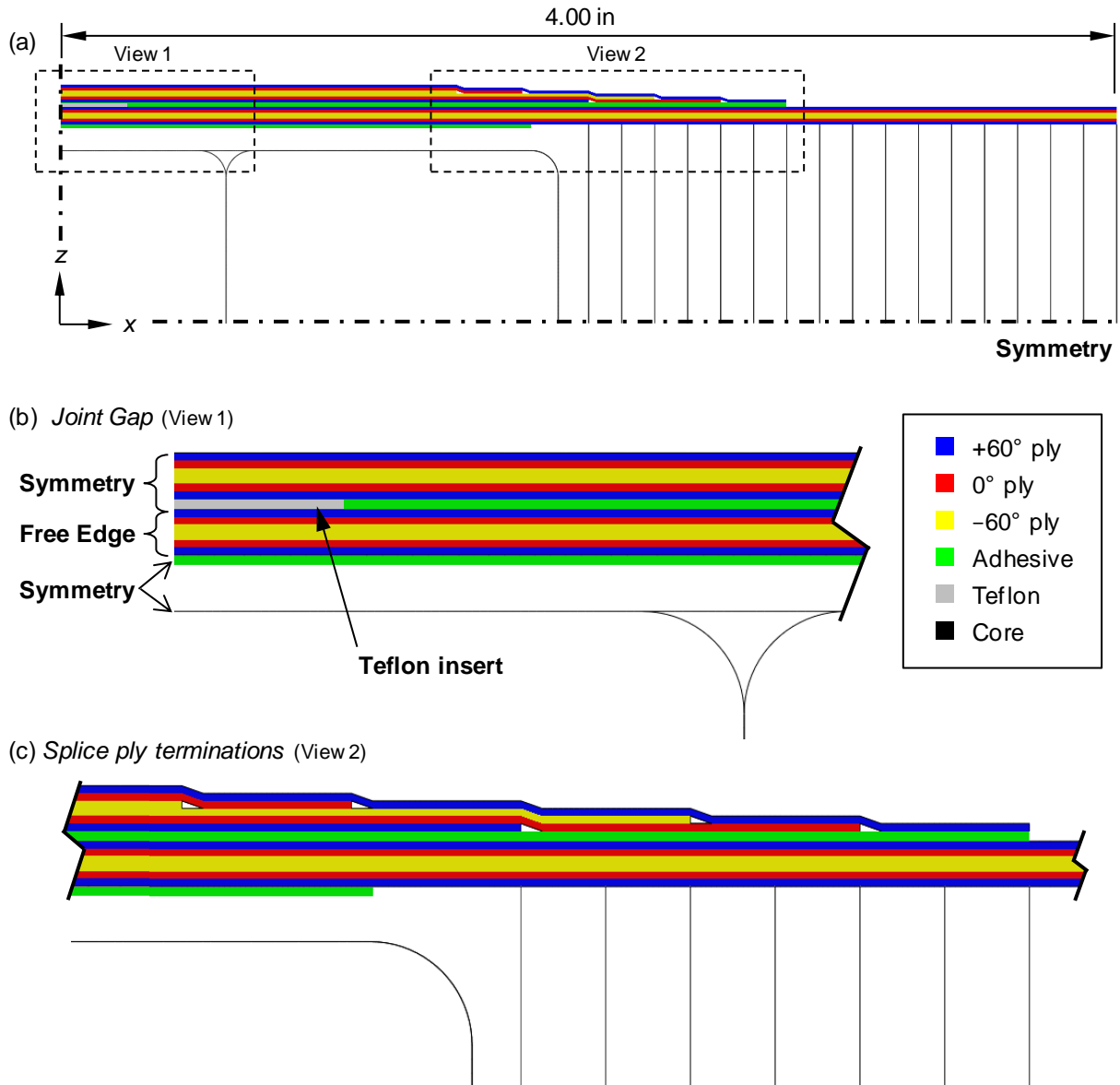


Figure 14. Cross-sectional view of the FE mesh for the durable redundant joint models.

For the tensile loading case, symmetry boundary conditions were applied along the splice plies and the DRJ inserts at the joint center ( $x = 0$  plane), leaving the facesheet nodes free, as shown in Figure 14b. For the compressive loading case, symmetry boundary conditions were applied for both the splice and facesheet nodes. As in the case of the CSJ models, symmetry was also assumed along the center lines of the honeycomb core and the DRJ inserts. In order to reduce the analysis times, the DRJ models were solved with a reduced width of 0.0975 inch (i.e., 13 elements). Loads were applied by uniformly displacing the right side of the facesheet and honeycomb core in the positive or negative  $x$ -direction for tensile and compressive loading, respectively.

## 6 Results of Bonded Composite Joint Models

### 6.1 Strength Predictions and Failure Mechanisms

For each of the specimens and loading cases that were analyzed, comparisons were made to the experimental results in terms of overall structural load-displacement and the manner in which damage evolves. For each of the experiments, load-displacement results were available. A summary of the experimental and computational failure loads are shown in Table 7. The experimental failure loads in Table 7 are the average of all tests performed for that specimen design and loading configuration. Damage was characterized experimentally by high-resolution digital cameras and DIC systems monitoring the top, bottom, and/or cross-sections of the specimens. Because of the unpredictability of the exact location and timing of damage initiation and evolution in experiments, direct comparisons between experiments and computational model results are limited. A complete discussion of the computational results and their comparisons with the experimental results is found in this section.

Table 7. Summary of Experimental and Predicted Failure Loads.

	Pristine		Conventional Splice		Durable Redundant	
	Test	Analysis	Test	Analysis	Test	Analysis
Tension [lbf]	26,261	35,509	24,948	28,010	30,394	31,190
Compression [lbf]	22,556	45,755	23,577	44,393	24,532	44,277

#### 6.1.1 Analyses of Pristine Sandwich Panels

Three loading cases were evaluated for the pristine sandwich panel model: extension along the 0° plies, compression along the 0° plies, and compression along the 90° plies. The same mesh was used for all three cases, with only the sign of the applied displacements and the material orientations being changed.

Due to the reduced dimensions of the pristine panel model, it was necessary to scale-up the loads and displacements for comparison with the experimental results. The loads in the tensile and compressive specimens were increased by scale factors equal to the ratio of the width of the full specimen to the width of the model and accounting for the quarter symmetry of the models. To obtain model displacements that can be compared to the experimental applied displacements, it was necessary to take into account the displacement along the length of the specimen that was not modeled. This additional displacement  $u^-$  is a function of the reaction load  $F$ , the length not included in the model  $L^-$ , the undamaged laminate stiffness  $k_{lam}$ , and the cross-sectional area of the laminate  $A$ , as represented by equation (5).

$$u^- = \frac{FL^-}{k_{lam}A} \quad (5)$$

The displacements used in the comparison with experimental results are equal to the sum of the applied model displacement and  $u^-$ . Because the displacement in the portion of the specimen that is not in the model is a function of the reaction load, this approach to scaling the displacements causes predicted load-drops to appear as snapbacks in the reduced structural load-displacement responses. For clarity, any such nonphysical snapbacks are plotted instead as unstable load drops. For the tensile and compressive

specimens,  $L^-$  values of 9.0 and 4.0 inches were used in the displacement scaling calculations, respectively.

***Pristine Sandwich Panel Subjected to Tension Loading (Pristine\_Tnsn)***

The analysis indicates that damage in the pristine sandwich panels starts at an applied load of approximately 14 kips in the +60° plies. At 22.7 kips, matrix cracking initiates in the two interior -60° plies. These cracks cause the subtle load drop visible in the load-displacement plot shown in Figure 15. After this point, widespread matrix cracking accumulates throughout the +60° and -60° plies until the predicted panel strength, which is 35.5 kips. It can be observed that the tensile strength of the specimen is approximately equal to the fiber tensile strength of the four 0° plies, i.e.:

$$(4 \text{ plies}) * (0.0075 \text{ in. thick}) * (3.0 \text{ in. wide}) * (378,000 \text{ psi}) = 34.02 \text{ kip}$$

Both of the pristine panel tensile specimens that were tested failed in the vicinity of the load grips, indicating that the pressure applied at the grips may have introduced unintentional stress concentrations, causing premature failure. As a result, there is no experimental data available for a direct comparison with failure load predictions. However, a good correlation between the experimental and computational in-plane stiffness was obtained.

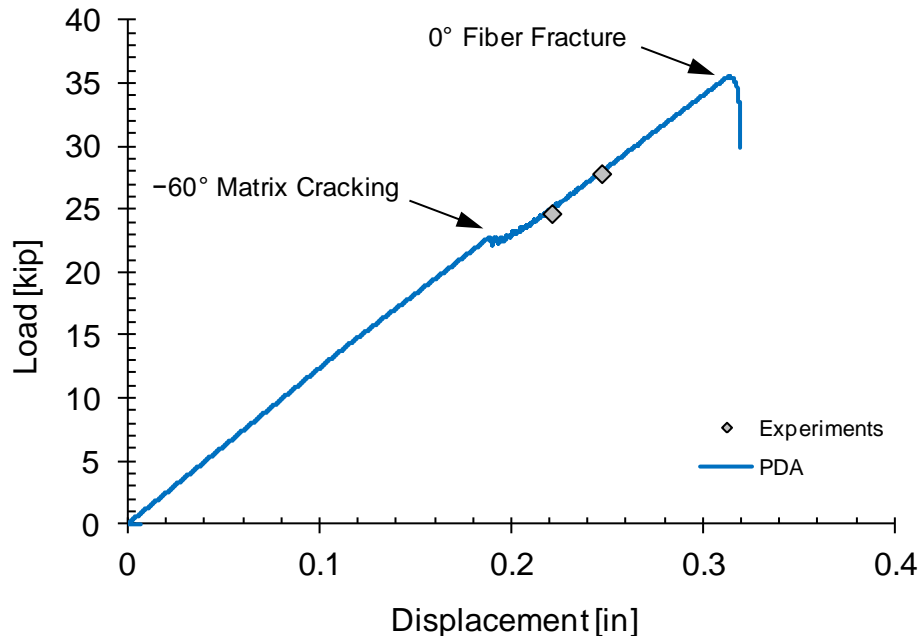


Figure 15. Load-displacement plot of the pristine panels subjected to tensile loading. The maximum predicted load was +35.5 kips.

***Pristine Sandwich Panel Subjected to Compression Loading in the 0°-Direction (Pristine\_Cmpr\_L)***

The analysis indicates that the response of the pristine specimen subjected to compressive loading is characterized by relatively a short period of damage evolution. Whereas the pristine tensile specimen was

predicted to undergo a long sequence of minor failures during its loading history, the compression specimen predictions exhibit sudden unstable damage propagation shortly after the initiation of the critical failure mechanism. No matrix cracking was predicted prior to the failure of the specimen.

The compressive fiber strength is reached throughout the  $0^\circ$  plies at approximately  $-49.0$  kips (i.e., the knee in the load-displacement plot of Figure 16). This point should correspond to the end of the test. However, due to the perfectly uniform loading and softening of the  $0^\circ$  fibers in the model, no local buckling or instabilities occur. Instead, a gradual softening of the load-displacement response occurs, corresponding to the softening of the  $0^\circ$  ply fiber stiffnesses. The length of the “plateau” in the response is related to the compressive fiber fracture toughness. Upon reaching approximately  $-60.9$  kips applied load, compressive matrix damage is predicted to initiate in the  $+60^\circ$  plies. The predicted compressive matrix damage is not uniformly distributed throughout the plies, causing local buckling in the facesheets and panel failure at  $-62.5$  kips. There is no experimental test data available for the compressive loading of the pristine panel in this configuration.

### ***Pristine Sandwich Panel Subjected to Compression Loading in the $90^\circ$ -Direction (Pristine\_Cmpr\_T)***

The load-displacement results for compressive loading in the  $90^\circ$ -direction are similar to those for loading in the  $0^\circ$ -direction shown in Figure 17. The panel responds linearly until the initiation of compressive fiber damage in the  $+60^\circ$  and  $-60^\circ$  plies at approximately  $-41.6$  kips applied load. Panel failure is predicted to occur at approximately  $-45.7$  kips as a result of interply delaminations that emanated from the specimen edges causing the facesheets to buckle. Two tests were conducted for this loading condition, yielding failure loads of  $23.1$  and  $22.0$  kips, much lower than the predicted results. However, it should be noted that these two test specimens failed within less than one inch of the loading grips, making any direct comparison of the experimental and computational failure loads invalid.

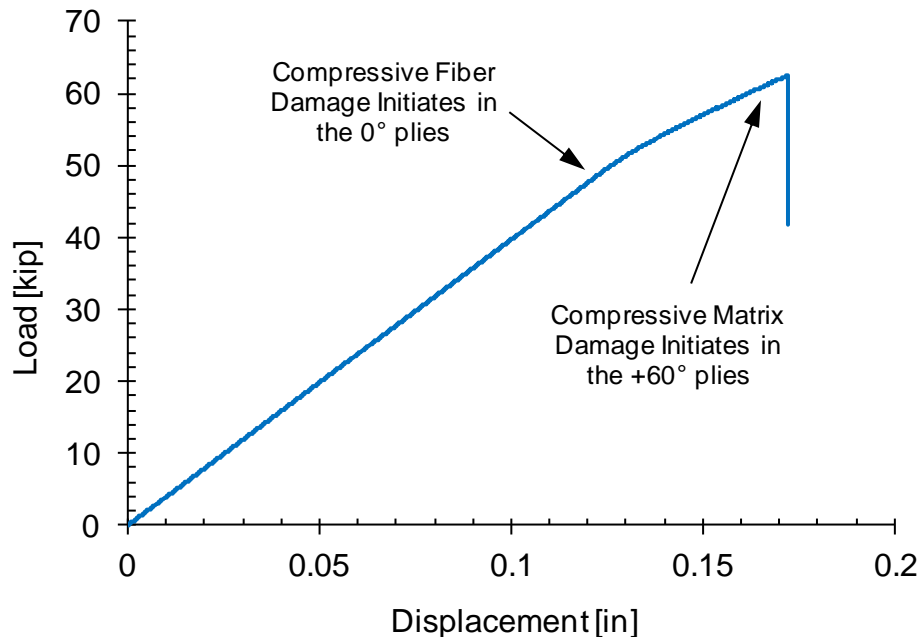


Figure 16. Load-displacement plot of the pristine panels subjected to compressive loading along the  $0^\circ$  direction. The maximum predicted load was  $-62.5$  kips.

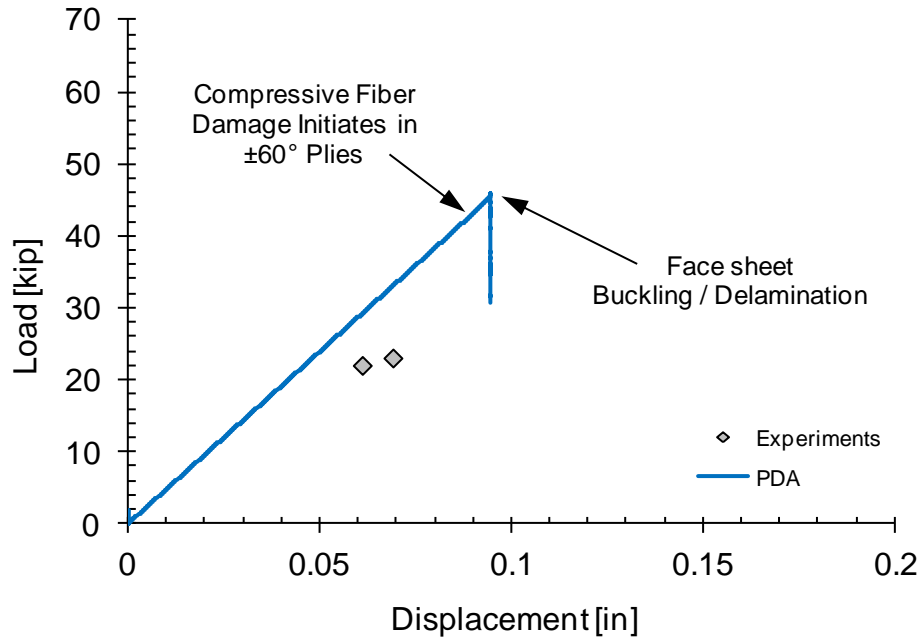


Figure 17. Load-displacement plot of the pristine panels subjected compressive loading along the 90° direction. The maximum predicted load was -45.8 kips.

## 6.1.2 Analyses of Conventional Splice Joints

### *CSJ Subjected to Tension Loading (CSJ\_Tnsn)*

Excellent correlation was observed between the experimental and computational results for the conventional splice joints subjected to tensile loading in terms of load-displacements results as well as the sequence of failures leading to ultimate specimen fracture. The predicted load-displacement curve for the CSJ tension specimen is shown in Figure 18. The predicted peak load of the tensile CSJ specimen is approximately 28.0 kips, compared to the experimentally observed strengths of 24.5 and 25.4 kips.

Prior to the predicted failure of the joint specimen, several instances of localized damage development occur in the model. At approximately 3.4 kips applied tensile load, prior to the prediction of any intraply or interply cracks, the adhesive layer begins to soften immediately ahead of the Teflon insert. The softening of the adhesive is a very gradual process, as expected due to the relatively large fracture toughness values determined during the material characterization work. As a result, no significant load redistribution occurs due to the initial softening of the adhesive, as is indicated in Figure 18.

Localized matrix cracking is predicted to occur at two “hot spots” in the CSJ model between 9 and 10 kips applied tensile load: in the top 60° ply of the facesheet near the termination of the last 0° splice ply, and in the bottom 60° ply of the splice near the end of the Teflon insert. These cracks initially have no effect on the global load-displacement response.

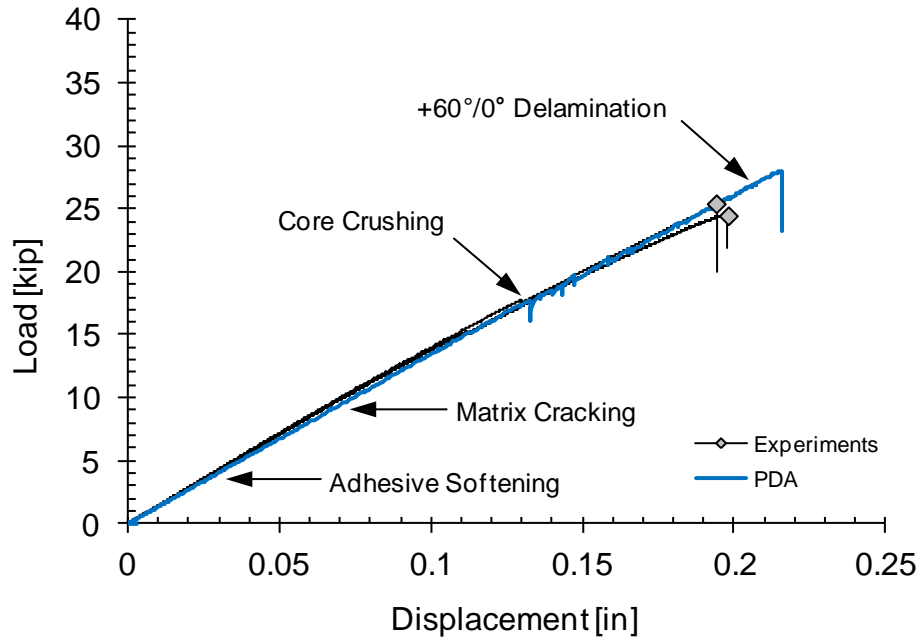


Figure 18. Load-displacement plots of the conventional splice joints subjected to tensile loading. The maximum predicted load was +28.0 kips.

The eccentricity in the load path due to the splices causes bending of the facesheet near the end of the Teflon insert, causing compressive loads in the honeycomb core in excess of its strength (300 psi). At an applied load of 17.6 kips, the core fails by buckling of the walls of the two rows of cells closest to the joint center (i.e., four in total, assuming symmetric damage), as shown in Figure 19a. This core crush failure mechanism was also observed experimentally, as shown in Figure 20. As with the pristine panel, widespread matrix cracking is predicted to initiate in the facesheet at 17.7 kips, causing a noticeable drop in the load-displacement response, as can be observed in Figure 18. At 27.6 kips, delaminations develop between the 60° and 0° plies at the locations of the first two 60° matrix cracks, as shown in Figure 19b. The delaminations at both locations are approximately 0.05 inch long at this load level. The delamination originating near the Teflon insert continues to grow to a length of 0.15 inch, when the peak load of 28.0 kips is reached, Figure 19c. Unstable delamination propagation ensues, eventually linking up with the delamination near the Teflon insert, cracking the matrix and adhesive where they meet.

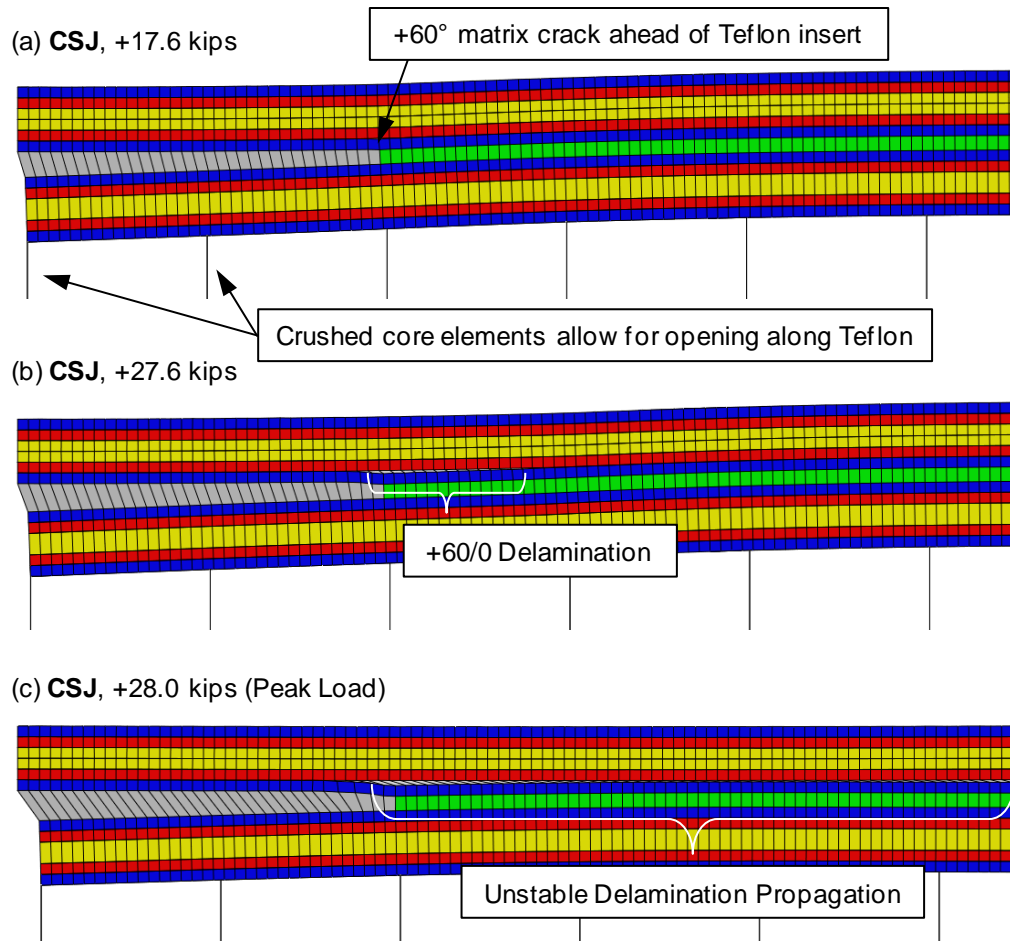


Figure 19. Failure process for conventional splice joint subjected to tensile loading.

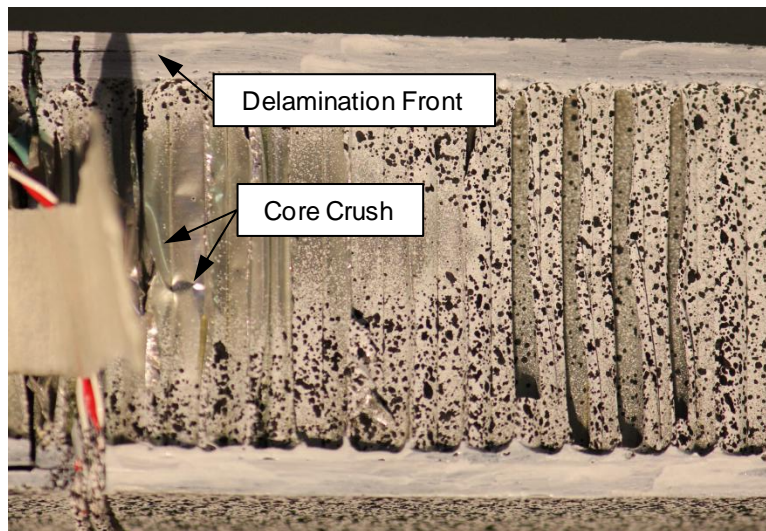


Figure 20. Digital photograph of a CSJ subjected to tensile loading. The crushed core and the separation of the facesheet and splice along the Teflon insert are clearly visible.

### *CSJ Subjected to Compression Loading (CSJ\_Cmpr\_L)*

The compressive CSJ model does not exhibit nearly as much damage development before the failure of the joint as the tensile CSJ model. No interply matrix cracks, delaminations, or softening of the adhesive layer are predicted to occur. Instead, the critical failure mechanism is buckling of the facesheets in the vicinity of the final two ply terminations. The eccentricity of the facesheet loads in this region causes the facesheets to bend and for compressive loads to develop in the honeycomb core. At -40.0 kips compressive applied load, the core begins to crush in this region, allowing for more significant bending of the facesheet, Figure 21. The facesheet is predicted to buckle at a peak load of -44.4 kips when the compressive fiber strength in the upper 0° facesheet ply is exceeded, Figure 22. It should be noted that while the crushed core at the predicted failure site affects the ability of the facesheets to resist buckling, the fiber compressive failure criterion is predicted to be equal to 0.96 when core crushing initiates. As a result, the prediction of joint failure in the compressive CSJ model should be nearly unaffected if core crushing was not considered.

This predicted peak load is significantly higher than the experimental results, which averaged -23.6 kips. It should be noted, however, that all three compressive CSJ test specimens failed within one inch of the tabbing. The effects of the tabbing were not considered in the progressive damage models. This being the case, the different failure mechanisms seen in the experimental and computational results are the result of different stress concentrations and should not be directly compared.

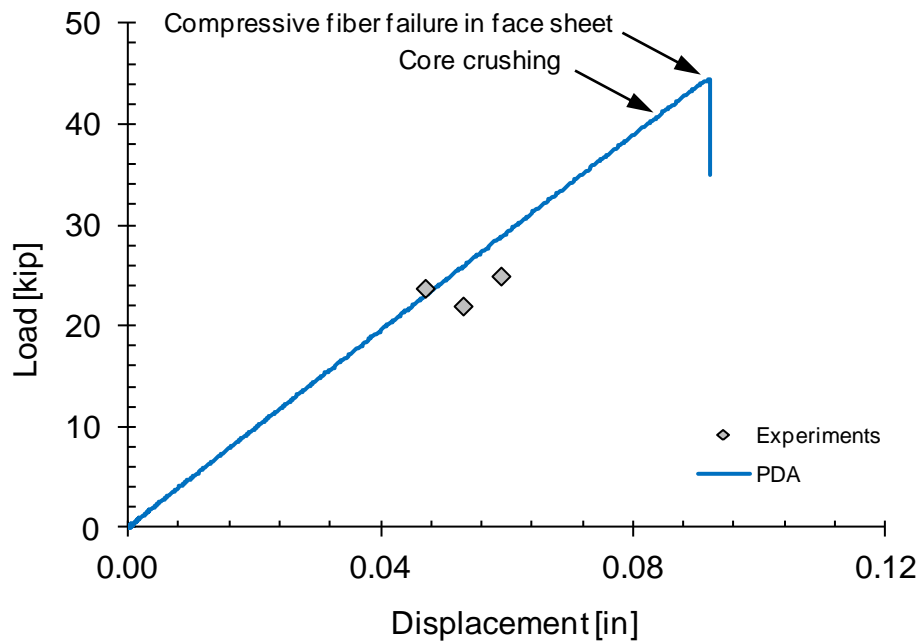


Figure 21. Load-displacement plots of the CSJ subjected to compressive loading. The maximum predicted load was -44.4 kips.

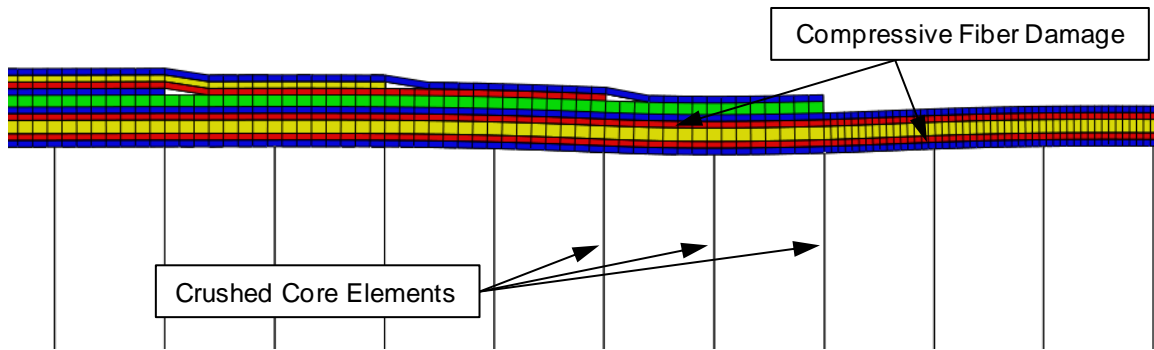


Figure 22. Buckling of the facesheet in the compressively loaded CSJ model.

### 6.1.3 Analyses of Durable Redundant Joints

#### *DRJ Subjected to Tension Loading (DRJ\_Tnsn)*

While the predicted sequence of damage mechanisms is very similar between the tensile CSJ and DRJ models, the inclusion of the DRJ inserts in the joint design moves the significant damage developments outside the reinforced region of the joint, as can be seen in Figure 23. In fact, no matrix cracks or adhesive damage is predicted in the doubly reinforced region prior to the predicted joint failure.

Matrix cracks form early at two locations in the facesheet: in the top  $60^\circ$  ply of the facesheet near the termination of the last  $0^\circ$  splice ply, and in the bottom  $60^\circ$  ply of the facesheet just outside the DRJ inserts. These two cracks occur at 8.9 and 13.7 kips, respectively, Figure 24. Softening of the adhesive layers between the splice and the facesheet and between the facesheet and the inserts starts at very low loads (i.e., 3.0 kips), but does not grow to a significant length before matrix cracking initiates. Widespread matrix cracking in the unbounded section of the facesheet occurs later, at 17.4 kips applied tensile load.

A delamination between the  $60^\circ$  and  $0^\circ$  plies of the facesheet near the ply terminations forms at 20.2 kips applied tensile load, Figure 25a. At this time, the region of softened adhesive extends approximately 0.04 inch from the termination of the  $0^\circ$  splice ply and 0.03 inch from the insert edge. This delamination propagates toward the joint center until reaching an approximate length of 0.06 inch at the peak load of 31.2 kips, Figure 24. At this point, the two softened adhesive regions extend 0.13 inch from the  $0^\circ$  ply termination and 0.95 inch from the insert edge, Figure 25b.

After reaching the peak load, damage propagates inward toward the Teflon insert (i.e., to the left in Figure 25c) from both the insert/facesheet interface and the ply termination delamination. These two damage fronts are predicted to independently link up with the Teflon insert, completely separating the facesheet from the inner and outer splices. Cracks originating at these two locations were observed experimentally while testing specimen Tnsn\_DRJ\_2, Figure 23.

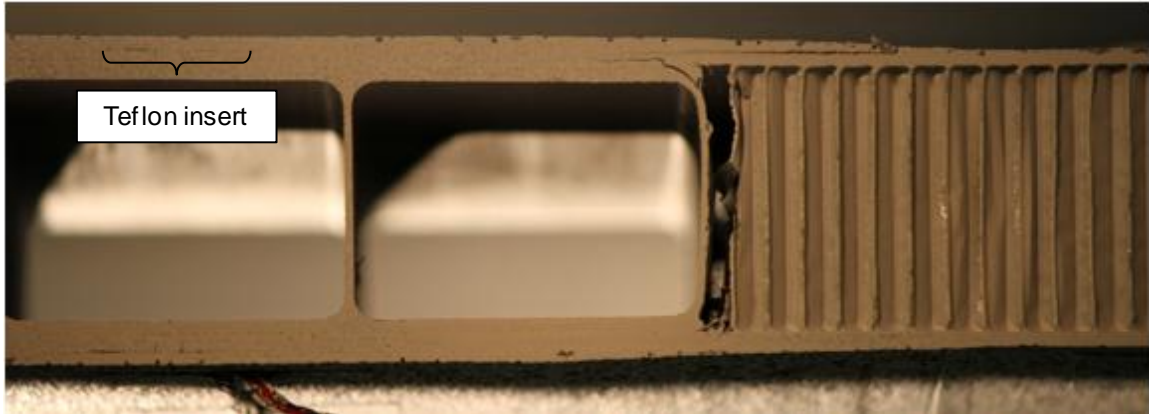


Figure 23. Digital photograph of cross-section of specimen DRJ\_Tnsn\_2, just prior to failure.

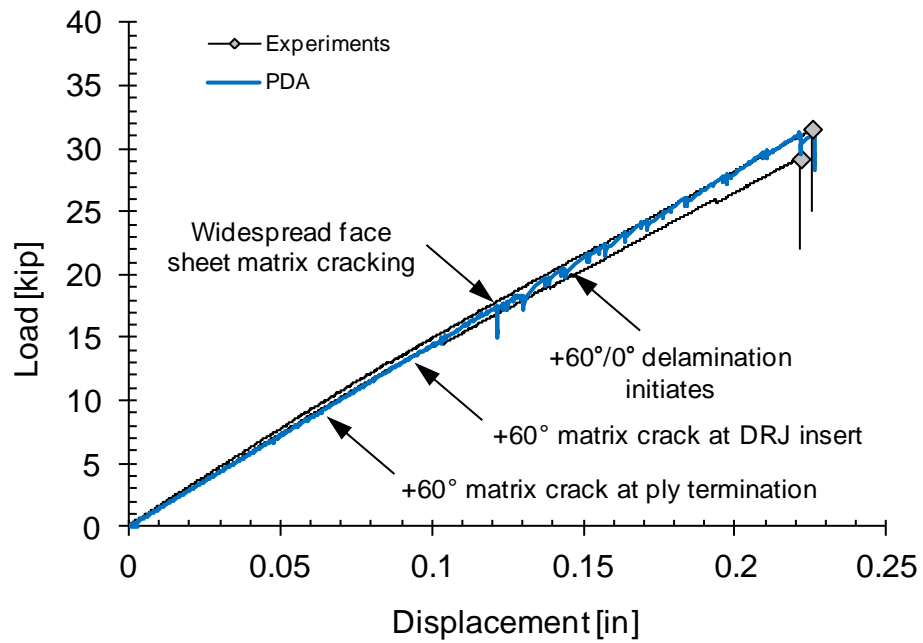


Figure 24. Load-displacement plot of the DRJ subjected to tensile loading. The maximum predicted load was +31.2 kips.

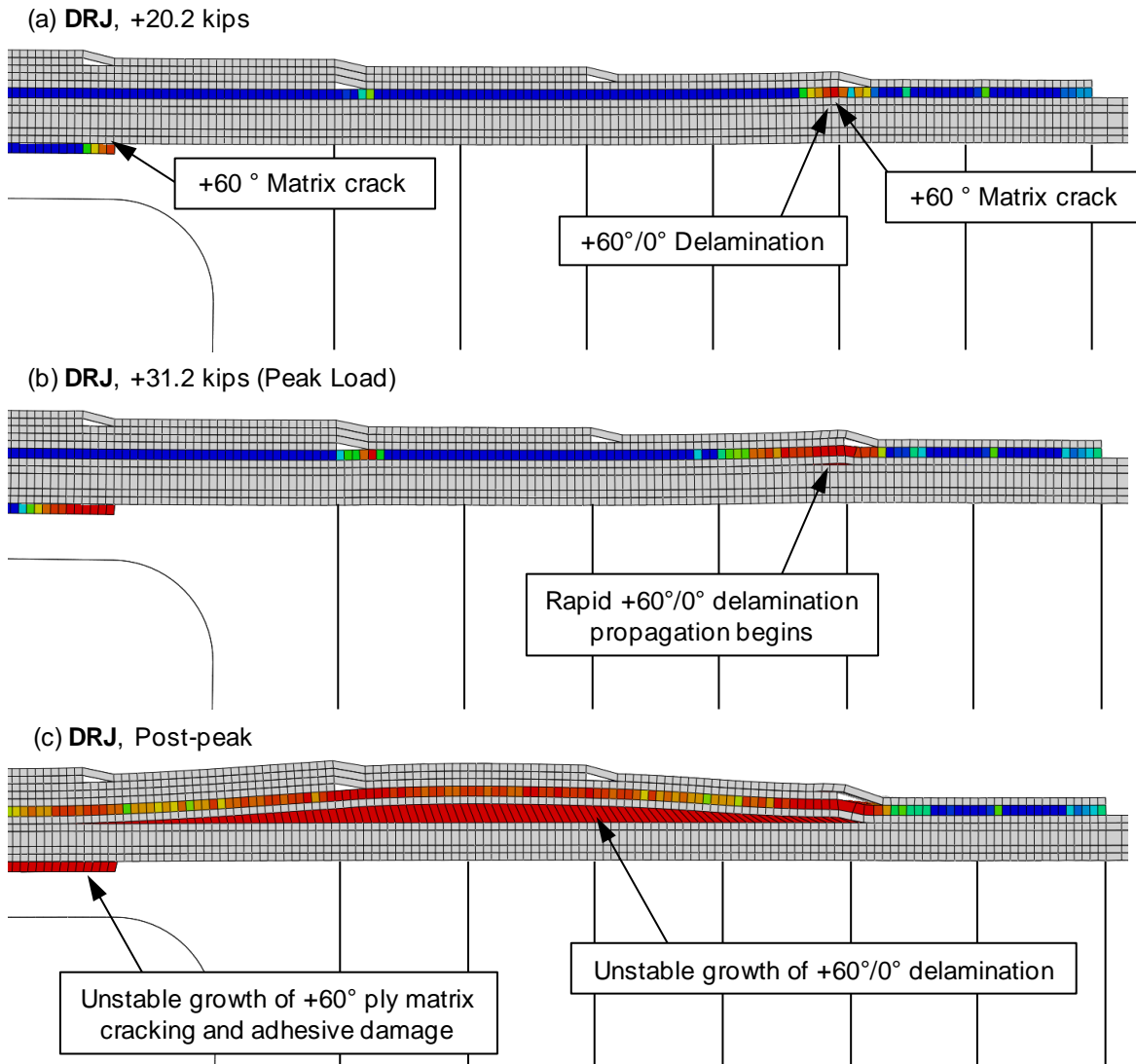


Figure 25. Failure process for the DRJ subjected to tensile loading. The adhesive and interply delamination damage variable is shown in the subplots, with blue representing intact material and red representing fully degraded elements.

### ***DRJ Subjected to Compression Loading (DRJ\_Cmpr\_L)***

The compressive DRJ results are very similar to the predicted CSJ model results. No significant matrix cracking or adhesive damage is predicted to occur prior to the failure of the joint specimen. Eccentricity of the facesheet / splice combination in the vicinity of the outer two ply terminations cause local bending and for compressive loads to develop in the honeycomb core. The compressive strength of the honeycomb core elements are exceeded at approximately  $-39.0$  kips applied load, crushing the core elements, Figure 26. The compressive fiber failure criterion is exceeded at  $-44.3$  kips in the upper  $0^\circ$  ply of the facesheet between the two outermost ply terminations. The imbalanced stiffness of the facesheet due to the softening of the  $0^\circ$  fibers then causes the facesheet to buckle, Figure 27.

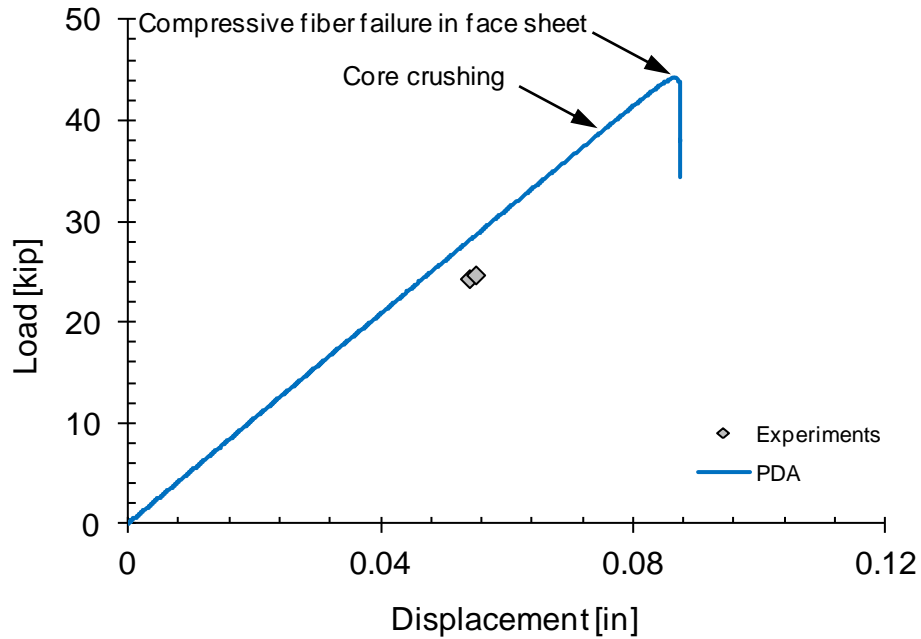


Figure 26. Load-displacement plot of the DRJ subjected to compressive loading. The maximum predicted load was -44.3 kips.

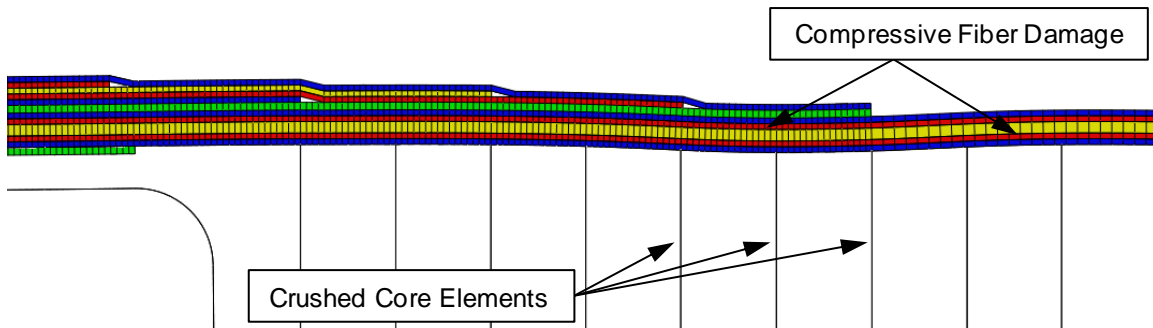


Figure 27. Buckling of the facesheet in the compressively loaded DRJ model.

## 6.2 Effect of the Teflon Insert Length on the Conventional Splice Joint Strength

A computational study was conducted on the effect of the length of the Teflon insert in the CSJ models on the predicted strength and failure mechanisms when subjected to tensile loading. The half-length of the Teflon insert in the CSJ model was increased in 0.125-inch increments from 0.000 to 0.500 inch. The parametric formulation of the finite element models required changing of only a single value in the model input. All other material properties and geometries were kept constant. The load-displacement results of this study are shown in Figure 28.

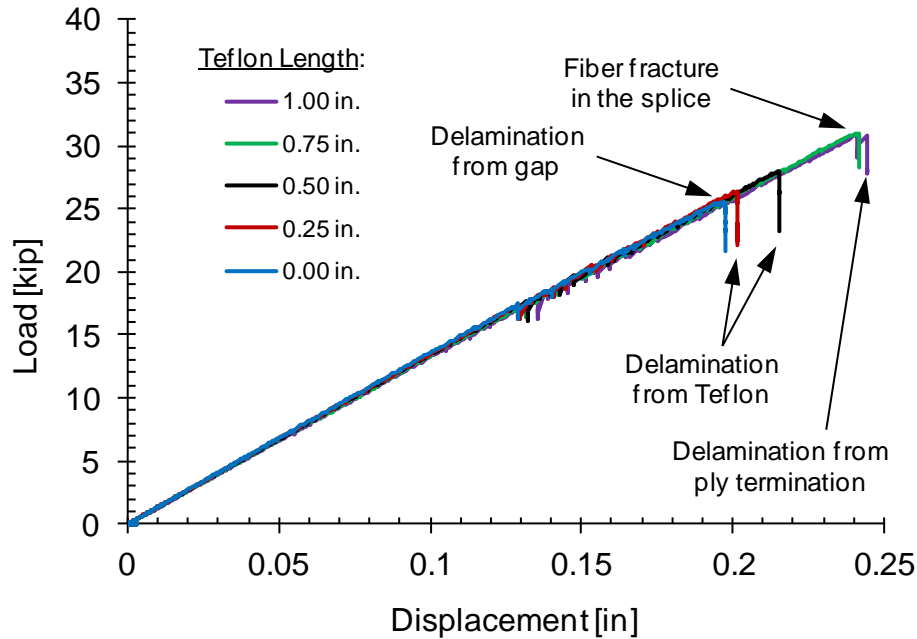


Figure 28. The predicted peak loads of the CSJ models for various Teflon insert lengths when subjected to tensile loading.

For the CSJ without Teflon insert and CSJ with a short 0.25-inch Teflon insert, the predicted failure mechanism remained unchanged from the 0.50-inch case: unstable  $+60^{\circ}/0^{\circ}$  delamination propagation from the center of the joint proceeded by matrix cracking and core crushing. However, shorter Teflon inserts (i.e., shorter initial cracks) cause less severe stress states in the adhesive layer, and, accordingly, less softening of the adhesive early in the simulation. When the adhesive layer softens in the models, it diminishes the severity of the interply stress concentration in the splice by transferring the load from the facesheet to the splice over a larger region, delaying the onset of matrix cracking and interply delamination. With less softening of the adhesive layer in the 0.00- and 0.25-inch Teflon models, the  $+60^{\circ}/0^{\circ}$  interface above the adhesive is more severely loaded, causing the delamination to form and propagate at lower applied loads of 25.6 and 26.4 kips, respectively.

The trend of longer Teflon inserts causing more extensive softening of the adhesive layer and, therefore, increasingly delayed onset of matrix cracking and delamination in the splice holds true for each of the Teflon lengths analyzed. However, while the peak  $+60^{\circ}/0^{\circ}$  interply loads in the splice decrease as the failure process zone of the adhesive develops, there is a stress concentration in the fiber direction of the bottom  $0^{\circ}$  ply of the splice, which is unaffected by the adhesive softening. This stress concentration is related to the bending of the splice in the vicinity of the Teflon insert due to the eccentricity of the load path through the facesheet / splice combination. The crushing of the core beneath the Teflon insert causes more bending in this region, which further increases the stresses in the fibers of  $0^{\circ}$  ply. In the case of the 0.75-inch Teflon insert model, fiber fracture is predicted in the  $0^{\circ}$  splice plies at this location at an applied tensile load of 31.0 kips. Because this failure mechanism is independent of the adhesive softening, it is expected that further increases in the Teflon insert length would not improve the joint performance. This is confirmed by the results of the 1.00-inch Teflon insert case. Interestingly, the 1.00-inch Teflon insert case fails at a peak load of 30.9 kips by a  $+60^{\circ}/0^{\circ}$  delamination originating near the outer  $0^{\circ}$  ply

termination in the facesheet (i.e., the predicted tensile DRJ failure mechanism). However, at the predicted peak load for the 1.00-inch Teflon, fiber damage is simultaneously developing in the 0° splice ply near the Teflon insert, indicating that the failures via fiber fracture and +60°/0° delamination from the ply termination are nearly coincident.

## 7 Closing Remarks

Progressive damage finite element analyses were conducted for two composite sandwich adhesively bonded joint designs to predict the load-displacement response and failure mechanism(s) and to compare the results with experimental results. The two tested joint designs consist of a conventional composite splice joint (CSJ) and a new NASA-patented durable redundant joint (DRJ) design. A series of experiments were conducted to determine strength and failure mechanism for each joint design under both tensile and compressive loads.

The nonlinear finite element analyses are capable of representing the initiation and evolution of several damage modes, including intraply fiber fracture, matrix cracking, interply delamination, adhesive failure, honeycomb core crushing, and their many potential interactions. All of the models used in the analyses of the joints are three-dimensional. However, the width and length considered by the models was reduced for computational efficiency. After optimization of the explicit analysis parameters, such as loading speed and mass scaling, analysis times of 2 to 8 hours were achieved on a desktop computer. In addition, all models were written parametrically to ensure that the model configuration, material properties, boundary conditions, etc. could be easily modified to perform parametric studies.

Excellent correlation was established between the experimental and computational results for the joint specimens loaded in tension. Both tensile specimens were predicted to exhibit a complex sequence of interacting failures, involving intraply matrix cracking, core crushing, adhesive softening, and interply delaminations. Though limited experimental data is available for comparison, studying the post-mortem photographs of the failed specimens indicates that the correct failure planes were predicted. In addition, the predicted failure loads for the CSJ and DRJ joints were within 13% of the experimental values.

The compressive joint specimens were predicted to fail due to facesheet buckling near the outside of the bonded regions. It was determined that the eccentricity of the load in this region caused sufficient bending of the facesheet to crush the honeycomb core and cause uneven softening of the facesheet 0° plies. Unfortunately, the experimental compressive specimens all failed in close proximity to the loading grips, not offering a direct source for comparison with the modeling predictions.

One of the major driving forces behind the development and application of new progressive damage analysis methods is the potential reduction of the experimental testing required to validate and optimize new structures and systems. By developing a sufficiently fine model and validating it for a few bounding cases, several intermediate values of design parameters can be evaluated quickly and cheaply. An example of the application of damage models for design optimization is performed, in which the parametric CSJ model is used to evaluate the sensitivity of the joint failure loads and failure mechanisms to the dimensions of a Teflon insert. With small variations of the length of this insert, three different critical failure mechanisms were observed, and an approximate 20% improvement in the predicted peak load of the joint was identified.

## References

---

- 1 Dávila CG, Camanho PP. Failure Criteria for FRP Laminates in Plane Stress. NASA/TM-2003-212663.
- 2 Pinho ST, Dávila CG, Camanho PP, Iannucci L, Robinson P. Failure Models and Criteria for FRP Under In-Plane or Three-Dimensional Stress States Including Shear Nonlinearity. NASA/TM-2005-213530.
- 3 Maimí P, Camanho PP, Mayugo J-A, Dávila CG. A Thermodynamically Consistent Damage Model for Advanced Composites. NASA/TM-2006-214282.
- 4 Leone FA, Dávila CG. (2011) Mixed-Mode Matrix Damage Evolution in Continuum Damage Mechanics. 16th International Conference on Composite Structures (1CCS16), Porto, Portugal.
- 5 Turon A, Camanho PP, Costa J, Dávila CG. (2006) A damage model for the simulation of delamination in advanced composites under variable-mode loading. *Mechanics of Materials* 38:1072–1089.
- 6 Ratcliffe JG, Czabaj, MW, Jackson, WC. A Model for Simulating the Response of Aluminum Honeycomb Structure to Transverse Loading. 2012 American Society for Composites 27th Technical Conference; 15th US-Japan Conference on Composite Materials Meeting. 1–3 Oct. 2012; Arlington, VA.
- 7 Boeing personal communication. (2012)
- 8 Reeder JR. (2006) 3D Mixed-Mode Delamination Fracture Criteria—An Experimentalist’s Perspective. 21st Annual Technical Conference of the American Society for Composites, Dearborn, MI.
- 9 Camanho PP, Maimí P, Dávila CG. (2007) Prediction of size effects in notched laminates using continuum damage mechanics. *Composites Science and Technology* 67:2715–2727.
- 10 Catalanotti G, Camanho PP, Xavier J, Dávila CG, Marques AT. (2010) Measurement of resistance curves in the longitudinal failure of composites using digital image correlation. *Composites Science and Technology* 70:1986–1993.
- 11 ASTM standard D 5528- 01 (2007) Standard Test Method for Mode I Interlaminar Fracture Toughness of Unidirectional Fiber-Reinforced Polymer Matrix Composites.
- 12 ASTM standard D 6671/D 6671M (2006) Standard Test Method for Mixed Mode I-Mode II Interlaminar Fracture Toughness of Unidirectional Fiber Reinforced Polymer Matrix Composites.
- 13 ASTM Work Item WK22949 (2009) New Test Method for Determination of the Mode II Interlaminar Fracture Toughness of Unidirectional Fiber-Reinforced Polymer Matrix Composites Using the End-Notched Flexure (ENF) Test.
- 14 Girolamo D. (2012) Progressive Damage Analysis of Composite Bonded Joints. MSc Thesis. TU Delft.
- 15 Breitzman TD, Iarve EV, Cook BM, Schoeppner GA, Lipton RP. (2009) Optimization of a composite scarf repair patch under tensile loading. *Composites: Part A* 40:1921–1930.
- 16 Reeder JR, Demarco K, Whitley KS. (2004) The use of doubler reinforcement in delamination toughness testing. *Composites: Part A* 35:1337–1344.
- 17 Balzani C, Wagner W, Wilckens D, Degenhardt R, Busing S, Reimerdes H-G. (2012) Adhesive joints in composite laminates – A combined numerical/experimental estimate of critical energy release rates. *International Journal of Adhesive & Adhesion* 32:23–38.

- 18 Benzeggagh ML, Kenane M. (1996) Measurement of mixed-mode delamination fracture toughness of unidirectional glass/epoxy composites with mixed-mode bending apparatus. *Composites Science and Technology* 56:439–449.
- 19 Rice JR. (1968) A path independent integral and the approximate analysis of strain concentration by notches and cracks. *Journal of Applied Mechanics* 35:145–153.
- 20 Leffler K, Alfredsson KS, Stigh U. (2007) Shear behaviour of adhesive layers. *International Journal of Solids and Structures* 44:530–545.
- 21 Högberg JL, Sørensen BF, Stigh U. (2007) Constitutive Behaviour of Mixed Mode Loaded Adhesive Layer. *International Journal of Solids and Structures* 44(25–26):8335–8354.
- 22 Turon A, Camanho PP, Costa J, Renart J. (2010) Accurate simulation of delamination growth under mixed-mode loading using cohesive elements: Definition of interlaminar strengths and elastic stiffness. *Composite Structures* 92:1857–1864.
- 23 Abaqus 6.10 Online Documentation, Dassault Systèmes, Providence, RI, USA, 2010.

**REPORT DOCUMENTATION PAGE**

*Form Approved  
OMB No. 0704-0188*

The public reporting burden for this collection of information is estimated to average 1 hour per response, including the time for reviewing instructions, searching existing data sources, gathering and maintaining the data needed, and completing and reviewing the collection of information. Send comments regarding this burden estimate or any other aspect of this collection of information, including suggestions for reducing this burden, to Department of Defense, Washington Headquarters Services, Directorate for Information Operations and Reports (0704-0188), 1215 Jefferson Davis Highway, Suite 1204, Arlington, VA 22202-4302. Respondents should be aware that notwithstanding any other provision of law, no person shall be subject to any penalty for failing to comply with a collection of information if it does not display a currently valid OMB control number.  
**PLEASE DO NOT RETURN YOUR FORM TO THE ABOVE ADDRESS.**

<b>1. REPORT DATE (DD-MM-YYYY)</b> 01-12-2012		<b>2. REPORT TYPE</b> Technical Memorandum		<b>3. DATES COVERED (From - To)</b>	
<b>4. TITLE AND SUBTITLE</b>  Progressive Damage Analysis of Bonded Composite Joints				<b>5a. CONTRACT NUMBER</b>	
				<b>5b. GRANT NUMBER</b>	
				<b>5c. PROGRAM ELEMENT NUMBER</b>	
<b>6. AUTHOR(S)</b>  Leone, Frank A., Jr.; Girolamo, Donato; Davila, Carlos, G.				<b>5d. PROJECT NUMBER</b>	
				<b>5e. TASK NUMBER</b>	
				<b>5f. WORK UNIT NUMBER</b>  794072.02.07.03.03	
<b>7. PERFORMING ORGANIZATION NAME(S) AND ADDRESS(ES)</b> NASA Langley Research Center Hampton, VA 23681-2199				<b>8. PERFORMING ORGANIZATION REPORT NUMBER</b>  L-20210	
<b>9. SPONSORING/MONITORING AGENCY NAME(S) AND ADDRESS(ES)</b> National Aeronautics and Space Administration Washington, DC 20546-0001				<b>10. SPONSOR/MONITOR'S ACRONYM(S)</b>  NASA	
				<b>11. SPONSOR/MONITOR'S REPORT NUMBER(S)</b>  NASA/TM-2012-217790	
<b>12. DISTRIBUTION/AVAILABILITY STATEMENT</b> Unclassified - Unlimited Subject Category 39 Availability: NASA CASI (443) 757-5802					
<b>13. SUPPLEMENTARY NOTES</b>					
<b>14. ABSTRACT</b>  The present work is related to the development and application of progressive damage modeling techniques to bonded joint technology. The joint designs studied in this work include a conventional composite splice joint and a NASA-patented durable redundant joint. Both designs involve honeycomb sandwich structures with carbon/epoxy facesheets joined using adhesively bonded doublers. Progressive damage modeling allows for the prediction of the initiation and evolution of damage within a structure. For structures that include multiple material systems, such as the joint designs under consideration, the number of potential failure mechanisms that must be accounted for drastically increases the complexity of the analyses. Potential failure mechanisms include fiber fracture, intraply matrix cracking, delamination, core crushing, adhesive failure, and their interactions. The bonded joints were modeled using highly parametric, explicitly solved finite element models, with damage modeling implemented via custom user-written subroutines. Each ply was discretely meshed using three-dimensional solid elements. Layers of cohesive elements were included between each ply to account for the possibility of delaminations and were used to model the adhesive layers forming the joint. Good correlation with experimental results was achieved both in terms of load-displacement history and the predicted failure mechanism(s).					
<b>15. SUBJECT TERMS</b>  Cohesive elements; Composites; Delamination; Fracture; Material characterization					
<b>16. SECURITY CLASSIFICATION OF:</b>			<b>17. LIMITATION OF ABSTRACT</b>	<b>18. NUMBER OF PAGES</b>	<b>19a. NAME OF RESPONSIBLE PERSON</b>
<b>a. REPORT</b>	<b>b. ABSTRACT</b>	<b>c. THIS PAGE</b>			STI Help Desk (email: help@sti.nasa.gov)
U	U	U	UU	47	<b>19b. TELEPHONE NUMBER (Include area code)</b>  (443) 757-5802